Mechanistic insight into substrate processing and allosteric inhibition of human p97

Man Pan[1#*], Yuanyuan Yu[1#], Huasong Ai[2], Qingyun Zheng[2], Yuan Xie[1], Lei Liu[2*], Minglei Zhao[1*]

[1] Department of Biochemistry and Molecular Biology, The University of Chicago, Chicago, IL 60637, USA.

[2] Tsinghua-Peking Center for Life Sciences, Department of Chemistry, Tsinghua University, Beijing 100084, China.

[#]These authors contributed equally to the work.

[*]Corresponding authors:

Minglei Zhao: mlzhao@uchicago.edu

Lei Liu: lliu@mail.tsinghua.edu.cn

Man Pan: panm@uchicago.edu

ABSTRACT

p97, also known as valosin-containing protein (VCP), processes ubiquitinated substrates and

plays a central role in cellular protein homeostasis. Mutations in human p97 are associated with

multisystem proteinopathy (MSP), a dominantly inherited degenerative disorder that can affect

muscle, bone and the central nervous system. It is also a drug target for cancer therapy with

various inhibitors developed over the past decade. Despite significant structural insights into the

fungal homologue of p97, Cdc48, little is known about how human p97 processes its substrates

and how the activity is allosterically affected by inhibitors. Here, we report a series of cryo-

electron microscopy (cryo-EM) structures of substrate-engaged human p97 complex with

resolutions ranging from 2.9 to 3.8 Å that captured "power stroke"-like motions of both the D1

and D2 ATPase rings of p97. The structures elucidated how the unfolded substrate is engaged

in the pore at atomic level. Critical conformational changes of the inter-subunit signaling (ISS)

motifs were revealed, providing molecular insights into substrate translocation. Furthermore, we

also determined cryo-EM structures of human p97 in complex with NMS-873, the most potent

p97 inhibitor, at a resolution of 2.4 Å. The structures showed that NMS-873 binds at a cryptic

groove in the D2 domain and interacts with the ISS motif, preventing its conformational change,

thus blocking substrate translocation allosterically. Finally, using NMS-873 at a

substoichiometric concentration, we captured a series of intermediate states, suggesting how

the cofactor Npl4 coordinates with the D1 ring of p97 to initiate the translocation.

44 **INTRODUCTION**

45   p97 is a 500 kDa protein that belongs to the family of ATPases Associated with diverse

46 cellular Activities (AAA)[1-3]. It undergoes repetitive ATP hydrolysis and conformational changes

47 to extract ubiquitinated substrates from various cellular components, such as membranes,

48 ribosomes, and chromatin[4]. p97 plays a central role in many cellular processes, including

49 endoplasmic reticulum-associated degradation (ERAD), mitochondrial-associated degradation,

50 chromatin-associated degradation, autophagy, and endosomal trafficking[5]. Mutations in human

51 p97 have been found in multisystem proteinopathy (MSP), a dominantly inherited degenerative

52 disorder that can affect muscle, bone and the central nervous system, that can manifest

53 clinically as inclusion body myopathy with early-onset Paget disease and frontotemporal

54 dementia (IBMPFD) and familial amyotrophic lateral sclerosis (ALS)[6,7]. Moreover, recent studies

55 have also targeted p97 for the treatment of cancer and viral infections[8,9].

56   p97 has two tandem AAA domains named D1 and D2 and an additional N domain at the

57 N-terminus (**Fig. 1a**). This protein functions as a homomeric hexamer, with twelve copies of

58 ATPase domains organized into two rings[10]. Crystal structures of full-length p97 were

59 determined more than a decade ago[11,12]. High-resolution single-particle cryo-electron

60 microscopy (cryo-EM) structures have also been reported[13,14]. However, all the structures of p97

61 determined thus far adopt a sixfold symmetric conformation, providing limited information

62 regarding the mechanism since almost all AAA proteins, including close homologues of p97,

63 break symmetry when engaged with substrates[15-17]. Recent cryo-EM studies of Cdc48, the

64 yeast homolog of p97, in complex with either in vivo[18] or in vitro[19] substrates provided crucial

65 insight into the working states. However, with medium resolution (3.7 Å to 4.2 Å) and limited

66 conformational states, critical mechanistic questions, such as how the AAA domains in two rings

67 coordinate to achieve translocation, remain to be answered. It is also not clear whether human

68 p97 shares the same mechanism as its yeast homologue. In addition, owing to its biomedical

69 importance, many small-molecule inhibitors of p97 have been developed in the past

70   decade[8,20,21]. Little is known regarding the allosteric inhibition mechanism due to the lack of a

71   p97 structure in a working state, which is of considerable biological and clinical interest.

72   In this study, starting from a fully assembled p97 complex with the cofactor Npl4/Ufd1

73   and a substrate, we triggered ATP hydrolysis and determined a series of substrate-engaged

74   p97 structures with resolutions ranging from 2.9 to 3.8 Å using single-particle cryo-EM. The

75   structures captured "power stroke"-like motions of both the D1 and D2 rings of p97 and

76   elucidated how the two rings coordinate to achieve translocation through the pore loops,

77   intersubunit signaling (ISS) motifs, and N- and C-terminal tails. We further determined the cryo-

78   EM structures of p97 in the presence of NMS-873, an allosteric noncompetitive inhibitor[21], at a

79   resolution of 2.4 Å and uncovered its inhibition mechanism. It is worth noting that NMS-873 has

80   been shown to be active in tumor cell lines and IBMPFD patient fibroblasts[21,22]. More

81   interestingly, low nanomolar concentrations of NMS-873 was recently reported to inhibit the

82   replication of several viruses, including severe acute respiratory syndrome coronavirus 2

83   (SARS-CoV-2) and influenza virus, through its inhibition on p97[23-25]. Finally, using NMS-873 at a

84   substoichiometric concentration, we captured a series of intermediate states, suggesting how

85   p97 coordinates with its cofactor Npl4 to initiate substrate translocation. Taken together, our

86   results established a comprehensive understanding of substrate processing and allosteric

87   inhibition of human p97.

88

89 **RESULTS**

90 **Capture the working states of human p97**

91 First, we assembled complexes of p97 from recombinantly overexpressed components

92 without introducing additional ATP. Two mutations, A232E and E578Q, were introduced into the

93 human p97 construct to stabilize the complex as previously described [26]. The A232E mutation is

94 found in MSP patients and is known as an activating mutant with its N domains locked in the "up

95 conformation"[27]. E578Q is a mutation in the Walker B motif of the D2 domain that slows

96 substrate unfolding[19,28]. Combined, the two mutations decreased but maintained the unfolding

97 activity of p97 (**Extended Data Fig. 1a**) and minimized the conformational heterogeneity

98 resulting from the N domains. All the structural work in this study used the p97 (A232E/E578Q)

99 mutant and Npl4/Ufd1 as the cofactors. For substrates, either polyubiquitinated Ub-Eos (Ub_n-

100 Eos) or K48-linked hexa-ubiquitin (Ub_6) was used. The assembled complex, named p97-

101 Npl4/Ufd1-Ub_n-Eos or p97-Npl4/Ufd1-Ub_6, eluted as single peaks in the size-exclusion

102 chromatograms (**Extended Data Fig. 1b and c**). To capture the working states of p97, ATP

103 hydrolysis was triggered by adding 5 mM ATP to the purified complexes followed by incubation

104 at room temperature for 5 minutes. To relieve the orientation preference, either CHAPSO or

105 fluorinated octyl maltoside (FOM) was added immediately before sample vitrification (**Fig. 1b**).

106 Three datasets, namely, p97-Npl4/Ufd1-Ub_n-Eos-CHAPSO, p97-Npl4/Ufd1-Ub_n-Eos-FOM, and

107 p97-Npl4/Ufd1-Ub_6-FOM, were collected, and a total of 9 different cryo-EM maps with

108 resolutions ranging from 2.9 to 3.8 Å were reconstructed using single-particle analysis

109 (**Extended Data Figs. 2-4, Extended Data Table 1**). Atomic models were built based on

110 existing p97 structures (**Extended Data Table 2**). For well-resolved regions, individual residues

111 were manually built into the density. For flexible regions, rigid body docking was used to fit

112 individual secondary structure elements or subdomains (see Methods for details).

113

114 **Open and closed states of the D2 ring**

115   In the p97-Npl4/Ufd1-Ub$_n$-Eos-CHAPSO dataset, two conformational states of the D2

116   ring were resolved (**Fig. 1c and d**). In the open state (3.6 Å, **Fig. 1c**, corresponding to class 2 in

117   **Extended Data Fig. 2**), all six D2 domains interacted with the substrate and formed an open,

118   right-handed spiral, whereas in the closed state (3.1 Å, **Fig. 1d**, corresponding to class 1 in

119   **Extended Data Fig. 2**), the bottom D2 domain (termed chain F) detached from the substrate

120   and shifted up to interact with the top D2 domain (termed chain E), closing the gap of the spiral

121   in the open state. Only five D2 domains (chains A-E) interacted with the substrate in the closed

122   state. The two states suggested a "power stroke"-like motion of the D2 domain (**Supplemental**

123   **Movie 1**). Compared to the same complex structure in the presence of ATPγS that was

124   previously published[26] (PDB ID: 7JY5), there was a relative 20 degree rotation of the D2 ring to

125   the D1 ring in both states (**Fig. 1e and Extended Data Fig. 5a**). A superimposition of the two

126   states showed that the D2 domain immediately above chain F (chain A) also shifted up from the

127   open state to the closed state (**Extended Data Fig. 6a** and **Supplemental Movie 1**). The

128   particles in the open state were significantly less than those in the closed state (13% vs. 70%),

129   suggesting that the open state is relatively transient. A third class was resolved from the 3D

130   classification (3.8 Å, class 3 in **Extended Data Fig. 2**), with better resolved density for the

131   cofactor Npl4 but otherwise the same conformation as the closed state.

132

133   **Conformational changes in the D1 ring**

134   In the p97-Npl4/Ufd1-Ub$_n$-Eos-FOM dataset, three conformational states of the D1 ring

135   were resolved (**Extended Data Fig. 3**). All the D2 rings were in the same conformation as the

136   closed state described above. Using the same naming convention, we discovered from the

137   superimposed structures that chain A shifted up slightly from class 1 (3.6 Å) to class 2 (3.4 Å)

138   and much further from class 2 to class 3 (3.0 Å) (**Extended Data Fig. 7a**). No open spiral

139   conformation similar to the open state of the D2 ring was observed for the D1 ring, although a

140   right-handed spiral was still formed by chains B-F. The three states of the D1 ring also

141   suggested a "power stroke"-like motion despite the differences from the D2 ring (**Supplemental**

142   **Movie 2**). It is worth noting that no conformational changes in the D1 ring were observed for the

143   p97-Npl4/Ufd1-Ub$_n$-Eos-CHAPSO dataset. The conformation of the D1 ring in the open and

144   closed states was very similar to class 3 of the p97-Npl4/Ufd1-Ub$_n$-Eos-FOM dataset (see

145   Discussion).

146

147   **Sequential but asynchronous hydrolysis in D1 and D2 rings**

148   The resolutions of the maps allowed us to build atomic models and identify the

149   nucleotides in most nucleotide binding sites (**Extended Data Figs. 6d and 7d**). For the less well

150   resolved chains A and F, the identity of the nucleotides could not be determined with certainty,

151   but the density of a nucleotide was clearly visible (**Extended Data Figs. 6d and 7d**). All

152   nucleotide binding sites were occupied, suggesting that the nucleotide exchange might be very

153   fast. When superimposing all the AAA domains within the same ring, two major conformations

154   were observed: one with a larger angle between the α/β and the α subdomain, potentially

155   corresponding to an ATP binding conformation, and the other with a smaller angle between the

156   α/β and the α subdomain, potentially corresponding to an ADP binding conformation (**Extended**

157   **Data Figs. 6c and 7c**). Such binary conformations have been observed for N-ethylmaleimide

158   sensitive factor (NSF), a close homologue of human p97[17].

159   When focusing on the well-resolved sites, we discovered a new compact ATP binding

160   mode in both the D1 and D2 rings involving a previously defined ISS motif[29]. Specifically, the

161   ISS motif changed from a helical conformation to a triangular loop that inserted into the

162   neighboring nucleotide binding site (**Fig. 1e and f**). L335 in the D1 domain and M611 in the D2

163   domain are the key residues interacting with the hydrophobic residues in the Walker B motifs of

164   the neighboring subunits (**Fig. 1f**). As a result, ATP is coordinated by three more residues than

165   the ATPγS-bound structure (PDB ID: 7JY5), including one additional arginine finger residue

166   (R362 in D1 and R638 in D2), an aspartic acid from the ISS motif (D333 in D1 and D609 in D2),

167   and a basic residue following the Walker A motif (R256 in D1 and K529 in D2) (**Fig. 1f**). This

168   binding mode was observed only when ATP was engaged and only for two to four consecutive

169   binding sites in both rings (**Fig. 1e**, **Extended Data Figs. 6b and 7b**). We hypothesize that this

170   tight binding mode results from rotational compression in ATPase rings essential for substrate

171   translocation. For ATP hydrolysis to occur, the ISS motif needs to be retracted. For example,

172   the ISS motif in the D2 domain of chain A retracted in the closed state (not in the open state)

173   since the neighboring D2 domain in chain B is the next subunit to undergo ATP hydrolysis (**Fig.**

174   **1e and Extended Data Fig. 6b**).

175   Another unexpected observation is that the hydrolysis in the D1 and D2 rings is not in

176   sync, which means that at a given time, the D1 and D2 domains of the same chain may engage

177   different nucleotides. If viewed from the top, hydrolysis propagates counterclockwise in both

178   ATPase rings, with the D1 ring one or two subunits ahead of the D2 ring (**Fig. 1e**). This feature

179   is unique for human p97 and has not been observed for other type II AAA proteins, including

180   yeast Cdc48.

181

182   **Interactions between the pore loops and the substrate**

183   In all six maps discussed above, we observed the density corresponding to a

184   translocating peptide going through the central pore of p97 (**Fig. 2a**). A continuous extended

185   peptide could be modeled into the density. The peptide went through the pore from the N-

186   terminus (bottom in **Fig. 2a**) to the C-terminus (top in **Fig. 2a**), as the other direction fit much

187   worse into the density. This directionality of translocating peptide is consistent with that of

188   Cdc48[19,30]. The density corresponding to the side chains was averaged, and polyalanine was

189   modeled.

190   In general, the density of the translocating peptide in the D2 ring was better than that in

191   the D1 ring. Three residues in pore loop-I (PL-I) of the D2 domain, namely, M550, W551, and

192   F552, interacted with the peptide like a "pitching grip" (**Fig. 2a**). Each PL-I formed two hydrogen

193   bonds with the nitrogen and carbonyl oxygen of one residue in the translocating peptide through

194   the carbonyl oxygen of M550 and nitrogen of F552. Every other residue in the translocating

195   peptide was hydrogen bonded by a PL-I so 12 residues were engaged with six PL-I in the D2

196   ring, which formed a spiral in the open state, with chain F at the bottom and chain E at the top

197   (**Fig. 2a**). In the closed state, the PL-I of chain F detached from the translocating peptide. The

198   remaining five PL-I formed the spiral in a very similar way except for the side chain of M550 in

199   chain A (now the bottom chain), which was pointing downwards and would not allow an

200   additional PL-I to engage (**Fig. 2a inset**). In both the open and closed states, the density of five

201   pore loop-II (PL-II) in the D2 ring was resolved (chains A to E) but at lower resolution (**Fig. 2a**

202   **inset**). PL-II in the D2 ring did not form hydrogen bonds with the translocating peptide and likely

203   played a less important role in translocation. We mutated the residues of PL-I and PL-II and

204   performed the substrate unfolding assay[1,26,31]. Indeed, the PL-I mutation (W551A/F552A)

205   abolished the unfolding activity, whereas the PL-II mutation (I590A/D592A) showed no effect

206   (**Fig. 2d**). A closer examination revealed that R599 was π-stacked with F552 of PL-I (**Fig. 2b**).

207   This interaction might be critical to stabilize the "pitching grip" conformation of PL-I since the

208   R599A mutant did not show any unfolding activity, similar to the PL-I mutation (**Fig. 2d**). In

209   contrast, the pore loops in the D2 domain of the nontranslocating structure (PDB ID: 7JY5) were

210   mostly unstructured (**Fig. 2c**).

211   PL-I in the D1 ring interreacted with the translocating peptide in the same fashion as that

212   in the D2 ring, except that only four PL-I (chains B-E) were engaged and the three residues

213   were K277, L278, and A279 (**Fig. 2a**). The "pitching grip" and hydrogen bonding pattern still

214   existed, but the interaction was not as strong as that of the D2 ring since the average length of

215   the hydrogen bonds was 3.9 Å in the D1 ring and 3.4 Å in the D2 ring. Two PL-II of the D1 ring

216   (chains C and D) were involved in the interaction with the peptide by forming a hydrogen bond

217   through H317 (**Fig. 2a**). Interestingly, H317 of chains B and C also stacked with W551 (PL-I of

218   D2) of chains D and E, respectively (**Fig. 2a**, red double arrow). This π-π stacking might be

219   involved in the coordination of two ATPase rings.

220   To further investigate the behavior of p97 with substrates of different sizes, we used a

221   much smaller substrate, Ub_6 (**Extended Data Fig. 1c**), and collected a third dataset, p97-

222   Npl4/Ufd1-Ub_6-FOM (**Extended Data Fig. 4**). Again, three conformations of the D1 ring that

223   were very similar to those of the p97-Npl4/Ufd1-Ub_n-Eos-FOM dataset were resolved.

224   Intriguingly, the density corresponding to the translocating peptide was resolved only in the D2

225   ring (**Fig. 2e**). The D1 ring was essentially void of the translocating peptide despite adopting the

226   same conformation. One possible explanation is that the D1 ring is engaged only when a

227   "complicated" substrate such as Ub_n-Eos is encountered.

228   We noticed that the D2 ring of the closed state is similar to one of the Cdc48 structures[30].

229   Both have five PL-I engaging with the translocating peptide. When the D2 rings from two

230   structures were superimposed, it was obvious that the two rings of p97 are out of register, that is,

231   the lowest D2 and D1 domains are not in the same chain (**Fig. 2f**), whereas in Cdc48, the two

232   rings essentially formed a single "split washer" (**Fig. 2g**). This out-of-register feature is

233   consistent with the asynchronous hydrolysis occurring in the D1 and D2 rings.

234

235   **N- and C-terminal tails and the linker between D1 and D2 rings**

236   In addition to the ATPase rings, some of the N- and C-terminal tails (**Fig. 1a**) of p97

237   were also resolved in the cryo-EM maps. Both the resolved N-terminal (L12 to R22) and C-

238   terminal (G767-S775) tails interacted with the neighboring subunit in a counterclockwise manner

239   if viewed from the top (N-terminal tail, **Fig. 3a**) or a clockwise manner if viewed from the bottom

240   (C-terminal tail, **Fig. 3c**). The N-terminal tail interacted with an acidic patch in the α subunit of

241   the D1 domain (**Fig. 3b**). The C-terminal tail interacted with a groove in the α subunit of the D2

242   domain. Such interactions have not been described before and may play important roles in the

243   coordination between different chains. Truncations of either the N- or C-terminal tails greatly

244   affected the unfolding activity of p97 (**Fig. 3f**). The linker between the D1 and D2 rings was

245   resolved for chains B-E. Compared to the structure of nontranslocating p97 (PDB ID: 7JY5), a

246   19 Å shift of L464 was observed (**Fig. 3e**). In the translocating structure, L464 interacted with

247   A569 in the D2 domain, which contributed to the relative twist of the D2 ring (**Fig. 1e**). The

248   L464A mutation decreased the unfolding activity of p97 (**Fig. 3f**). Notably, the N- and C-terminal

249   tails and the linker regions are less conserved between human p97 and yeast Cdc48, which

250   might contribute to the different conformations of the ATPase rings.

251

252   **NMS-873 inhibits the translocation by locking the ISS motif**

253   Inhibition of p97 has emerged as a promising strategy in anticancer and antiviral studies[8].

254   NMS-873, the first discovered noncompetitive inhibitor of p97 (**Fig. 4a**), was recently

255   characterized as a candidate for the treatment of cancers, neurodegenerative diseases, and

256   viral infections[22-24]. However, the mechanism of inhibition remained unclear. We introduced

257   NMS-873 at saturation (80 µM) after triggering ATP hydrolysis and substrate translocation (**Fig.**

258   **4b**). Two datasets were collected using Ub_n-Eos and Ub_6 as the substrate. A single map was

259   obtained from each dataset with overall resolutions of 2.4 Å (Ub_6, **Extended Data Fig. 8**) and

260   2.8 Å (Ub_n-Eos, **Extended Data Fig. 9**). The two maps are essentially identical; therefore, only

261   the map with the higher resolution is shown (**Fig. 4c**). NMS-873 binds at a cryptic groove next to

262   the ISS motif of the D2 domain (**Fig. 4d**) and is surrounded by many hydrophobic residues (**Fig.**

263   **4e**). Through the interaction with the alkyl chain of K615, NMS-873 locked the ISS motif and

264   prevented the essential conformational change discovered in the translocating structures (**Fig.**

265   **4f**). As a result, no translocating peptides were found in the central pore, and the structure was

266   6-fold symmetric, although a substrate was present, and ATP hydrolysis was triggered before

267   adding NMS-873.

268   Compared to the ATPγS-bound nontranslocating structure (PDB ID: 7JY5), the relative

269   positions of the ATPase rings in the NMS-873-bound structure are similar (**Extended Data Fig.**

270   **5b**). The bottom opening of the D2 ring was expanded, which is similar to that of the ADP-bound

271   structures[13], although ATP was engaged (**Extended Data Fig. 5c**). The pore loops in the D2

272   domain of the NMS-873-bound structure were resolved but retracted from the pore compared to

273   the translocating structure (**Extended Data Fig. 5e**). The smaller angle between the α/β and the

274   α subdomains suggested that it is more similar to an ADP-bound state (**Extended Data Fig. 5d**).

275   Indeed, superimposing the NMS-873-bound structure with another inhibitor-bound structure

276   (UPCDC30245, PDB ID: 5FTJ [13]) showed surprising similarities, including the conformations of

277   pore loops and a shared binding pocket of the two inhibitors in the D2 domain (**Extended Data**

278   **Figs. 5f and 5g**). The difference is that the UPCDC30245-bound structure was determined in

279   the presence of ADP without a cofactor and a substrate, and the compound was not fully

280   resolved in the cryo-EM map[13]. Importantly, the interaction between K615 and the biphenyl

281   group of NMS-873, which essentially locks the ISS motif, does not occur in the UPCDC30245-

282   bound structure (**Fig. 4f and Extended Data Fig. 5g**). Previous studies found that

283   UPCDC30245, a phenyl indole amide-based allosteric inhibitor, is an uncompetitive inhibitor and

284   binds only in the presence of ADP, whereas triazole-based NMS-873 is a noncompetitive

285   inhibitor and can bind in the absence of nucleotides[21]. This locking mechanism of NMS-873

286   through K615 might be the key for noncompetitive allosteric inhibition.

287

288   **Conformational states of Npl4 revealed by NMS-873 at a substoichiometric concentration**

289   We further discovered that NMS-873 did not fully inhibit the unfolding activity of p97 at a

290   substoichiometric concentration (6 equivalents (eq) is the stoichiometric concentration, **Fig. 4g**).

291   On the reasoning that intermediate structures could be captured using NMS-873 as a modulator,

292   a dataset was collected following the same protocol using Ub_n-Eos as the substrate and in the

293   presence of 10 μM NMS-873 (~0.2 eq, **Fig. 5a**). As expected, multiple intermediate structures

294   were resolved after 3D classification (**Extended Data Fig. 10**). Two out of six maps (~11%

295   particles) are in the nontranslocating state, with flat and symmetric ATPase rings and no density

296 for a translocating peptide (**Fig. 5c**). One of the nontranslocating maps (Class 1, ~8% particles)

297 showed the density of NMS-873 (**Fig. 5c**, top) in all six binding pockets, suggesting that the

298 binding of NMS-873 is highly cooperative. The cofactor Npl4 was resolved in four out of six

299 maps (**Extended Data Fig. 10**). Both nontranslocating maps showed density for Npl4, with

300 either one or two of its zinc finger motifs (ZF1 and ZF2, **Fig. 5b**) binding on top of the D1 ring

301 (**Fig. 5c**). Such seesaw conformations of Npl4 have been described in a previous study[26]. The

302 four translocating structures all had spiral ATPase rings and a translocating peptide similar to

303 the conformation of the closed state (**Extended Data Fig. 10**). Two maps (class 5 and class 6)

304 had very poor densities of Npl4 and differed in the D1 ring in a similar way to class 1 and class 3

305 of the p97-Npl4/Ufd1-Ub$_n$-Eos-FOM dataset. The other two maps showed density for Npl4, but

306 with its zinc finger motifs interacting with different chains (**Fig. 5d**), suggesting a rotation of Npl4

307 on top of the D1 ring. Although the resolution of Npl4 is not sufficient for atomic model building,

308 a trace density connected to the translocating peptide can be seen to be engaged in a groove of

309 Npl4 (**Fig. 5d**, top), which is reminiscent of a substrate processing complex structure of Cdc48[19].

310

311 **DISCUSSION**

312   Here, we report the cryo-EM structures of human p97 in several working states, with a

313 translocating peptide going through the central pore. Together, the structures revealed "power

314 stroke"-like conformational changes in both the D1 and D2 rings. Surprisingly, the two AAA

315 domains undergoing power stroke motion in each ring were not from the same chain, which

316 seemed to be a unique feature of human p97 and was not observed for Cdc48 and other Type-II

317 AAA proteins[15,16,19,30,32,33]. The unusual structural feature corresponds to the asynchronous

318 hydrolysis taking place in the two ATPase rings (**Fig. 1e**). Regarding translocation, the D2 ring

319 seemed to play a more important role by tightly interacting with the peptide through backbone

320 hydrogen bonds. The D1 ring was engaged when encountering a much larger substrate.

321 Previous biochemical studies have shown that the D2 ring of p97 had higher ATPase activity

322 and provided the driving force for translocation, which is consistent with our structures[34]. The

323 structures of Cdc48 also showed fewer interactions between the translocating peptide and the

324 pore loops of the D1 ring[19], further supporting this hypothesis. Although the structures strongly

325 support a sequential hydrolysis model[35], it is not clear whether the power strokes in the D1 and

326 D2 rings take place concurrently. Multiple structures from a single dataset are needed to

327 address this question. In this study, the motions of the D1 and D2 rings were resolved from two

328 datasets, one using CHAPSO and the other using FOM as the detergent to fix the orientation

329 preference. CHAPSO required a much higher concentration of the complex than FOM (8x) to

330 keep the samples in the hole but seemed to preserve the complex better and yielded more

331 particles with Npl4. Since the open state is a minor conformation (7% of the total particles,

332 **Extended Data Fig. 2**), the higher concentration of the CHAPSO dataset may have contributed

333 to its discovery.

334   The cryo-EM structures of human p97 in complex with NMS-873 revealed the

335 mechanism of allosteric inhibition by locking the ISS motif in the D2 domain, which together with

336 the ISS motif in the D1 domain played critical roles in forming the compressed ATPase rings

337   essential for substrate translocation (**Fig. 1f**). Targeting the ISS motif of p97, therefore, may

338   serve as a potential strategy for the development of new inhibitors.

339   Multiple structures in the presence of NMS-873 at a substoichiometric concentration

340   suggested that Npl4 may play a critical role in the initiation of translocation by unfolding the

341   ubiquitin chain and threading it into the central pore through a seesaw motion. The pore loops in

342   the D1 and D2 rings catch the thread-in peptide, and the two rings are compressed to spiral

343   conformations. Following sequential ATP hydrolysis and power stroke motions circulating in

344   both rings, the peptide in the pore is translocated downward. Npl4 might be unnecessary once

345   the translocation starts.

346   Mutations in p97 have been linked to MSP[6,36]. Structures of p97 in working states

347   provided crucial insights into the consequences of the mutations (**Extended Data Table 3,**

348   **Supplemental Movie 3**). The resolutions of the cryo-EM maps in this study are among the

349   highest of type II AAA proteins[15,17,19,30,33,37], allowing a comprehensive understanding of

350   substrate processing and allosteric inhibition of human p97 and shedding light on the

351   mechanism of other type II AAA proteins.

352

353 **METHODS**

354 **Protein expression and purification**

355 Wildtype human p97, human p97 mutants, Npl4/Ufd1, His_6-Ub^{G76V}-Ub^{G76V}-mEos3.2 (Ub-

356 Eos), human UBA1, Ube25k and gp78RING-Ube2g2 were purified as previously

357 described[26,31,38]. Briefly, all proteins were expressed in *E. coli* BL21(DE3) cells and purified

358 through Ni-NTA resin at 4 °C. All purified proteins were further buffer-exchanged to the Storage

359 Buffer containing 50 mM HEPES, pH 8.0, 150 mM NaCl, 1 mM $MgCl_2$, 0.5 mM tris(2-

360 carboxyethyl)phosphine (TCEP) before snap freezing.

361

362 **Preparation of polyubiquitinated Ub-Eos and polyubiquitin chain**

363 For cryo-EM studies, His-tagged Ub-Eos was directly used for polyubiquitination. For the

364 substrate unfolding assay, Ub-Eos was first irradiated under LED UV light (385-395 nm,

365 uvBeast V2) for 1 hour at 4 ºC to induce the photoconversion of mEos3.2, followed by

366 polyubiquitination. The polyubiquitination reaction was performed as previously described[31].

367 Briefly, 20 µM Ub-Eos was mixed with 1 µM UBA1, 20 µM gp78RING-Ube2g2, and 500 µM

368 ubiquitin in the Ubiquitination Buffer containing 20 mM Hepes, pH 7.4, 150mM KCl, 10 mM ATP,

369 and 10 mM $MgCl_2$. After incubation at 37 ºC overnight, the mixture was incubated with Ni-NTA

370 resin to remove free ubiquitin chains. The elution was further separated using a Superdex 200

371 (GE Healthcare) size-exclusion column equilibrated in the Storage Buffer. Polyubiquitinated Ub-

372 Eos (Ub_n-Eos) with longer ubiquitin chains (estimated over 10 ubiquitin subunits) was collected

373 and flash frozen for the substrate unfolding assay.

374 K48-linked polyubiquitin chains were assembled by mixing 1 µM UBA1, 10 µM Ube25k,

375 and 1 mM ubiquitin in the Ubiquitination Buffer at 37 ºC for 4 hours. The reaction mixture was

376 then diluted 10 folds with 50 mM NaOAc, pH 4.5, and separated by a Mono S cation exchange

377 column. The corresponding peak for hexa-ubiquitin chain (Ub_6) was collected and further

378   purified with a Superdex 75 (GE Healthcare) size-exclusion column equilibrated in the Storage

379   Buffer.

380

Assembly of substrate-engaged p97 complex

382   p97-Npl4/Ufd1 complex was assembled as previously described[26]. A p97 mutant bearing

383   A232E and E578Q mutations was used in order to decrease the heterogeneity of N domains

384   and reduce the unfolding activity of the complex. Two-fold molar excess of Ub_6 or Ub_n-Eos was

385   added to the p97-Npl4/Ufd1 complex, followed by gel filtration using a Superose 6 column (GE

386   Healthcare) equilibrated in the Storage Buffer (**Extended Data Fig. 1b and 1c**). The assembled

387   substrate-engaged p97 complex was flash frozen in liquid nitrogen for structural studies. No

388   nucleotide was supplemented during the assembly.

389

Specimen preparation for single-particle cryo-EM

391   All samples for cryo-EM were prepared as previously described[26], with the following

392   modifications. Either fluorinated octyl maltoside (FOM) or CHAPSO was used to relieve the

393   preferred orientations instead of IGEPAL CA-630. The complex was concentrated to ~2.5

394   mg/mL followed by incubation with 5 mM ATP at room temperature for 5 minutes before adding

395   FOM (final concentration 0.01% v/v, Fig. 1b). Glow discharged Quantifoil Cu 1.2/1.3 grids were

396   used for FOM supplemented samples. Alternatively, the samples were concentrated to

397   ~20mg/mL followed by incubation with 5 mM ATP at room temperature for 5 minutes before

398   adding CHAPSO (final concentration 4 mM, Fig. 1b). Non-glow-discharged Quantifoil Cu 1.2/1.3

399   grids were used for CHAPSO supplemented samples. In both cases, 3.5 μL sample was applied

400   to the grid and was blotted for 1 second using standard Vitrobot filter paper (Ted Pella, 47000-

401   100) before plunge freezing in liquid ethane. For substrate-engaged p97-Npl4/Ufd1 complex in

402   the presence of NMS-873, besides the aforementioned procedures, NMS-873 was

403   supplemented right after the incubation with ATP at either 10 μM or 80 μM final concentration.

404   The samples were incubated for another 30 min at room temperature before adding the

405   detergents and plunge freezing (Fig. 4b and 5a).

406

407   **Data collection for single-particle cryo-EM**

408   Data collection was performed either in Advanced Electron Microscopy Facility at the

409   University of Chicago or National Cryo-Electron Microscopy Facility at the National Cancer

410   Institute. All datasets were acquired as movie stacks with a Titan Krios electron microscope

411   operating at 300 kV, equipped with either a Gatan K2 Summit or K3 direct detector camera. A

412   single stack typically consists of 40 frames with a total exposure around 50 electrons/Å^2. The

413   defocus range was set at -1.0 to -2.5 μm. See **Extended Data Table 1** for the details.

414

415   **Image processing**

416   Movie stacks were subjected to beam-induced motion correction using MotionCor2[39].

417   CTF parameters for each micrograph were determined using CTFFIND4[40]. Particle picking, two-

418   and three-dimensional classifications, three-dimensional refinement, and local resolution

419   estimation were performed in RELION-3[41]. Particle picking was performed by manually

420   choosing ~2,000 particles and generating templates through reference free 2D classification,

421   followed by automatic template based picking. False-positive particles or particles classified in

422   poorly defined classes were discarded after 2D classification. The initial 3D classification was

423   performed on a binned dataset with the previously reported p97 structures as the reference

424   model[26]. The detailed data processing flows are shown in Extended Data Figs. 2, 3, 4, 8, 9, and

425   10. To make sure that the 3D classification did not miss any major conformations, additional

426   runs were performed with different number of classes (ranges from 3-8) and different

427   regularization parameters (ranges from 2-6). Since we did not observe a dependence on the

428   regularization parameter, the results from the default value (T=4) were shown in the figures.

429   Data processing statistics are summarized in **Extended Data Table 1**. Reported resolutions are

430   based on Fourier shell correlation (FSC) using the FSC=0.143 criterion.

431

432   **Model building, refinement, and validation**

433   Model building was based on the existing cryo-EM structures of human p97[26] (PDB ID:

434   7JY5). The models of individual domains (N, D1, and D2) were first docked into the cryo-EM

435   maps as rigid bodies using UCSF Chimera[42] followed by further adjustment using COOT[43]. For

436   well-resolved regions, sharpened maps were used and individual residues were manually

437   adjusted and fit into the density. For flexible regions, unsharpened maps were used and

438   individual secondary structure elements or subdomains were fit into the density as rigid bodies.

439   A short β strand was automatically built into the density corresponding to the translocating

440   peptide using COOT, followed by manual extension on either ends and real-space refinement

441   until the all the density was covered. The final models were subjected to global refinement and

442   minimization in real space using the real-space refinement module in Phenix[44]. Model validation

443   was performed using the comprehensive validation tool in Phenix. The statistics of model

444   refinement is shown in **Extended Data Table 2**.

445

446   **Substrate unfolding assay**

447   Substrate unfolding assay was performed as previously described[26,31]. Briefly, 20 nM

448   photoconverted polyubiquitinated Ub-Eos was mixed with 400 nM p97 or p97 mutants and 500

449   nM Npl4/Ufd1 in the Assay Buffer containing 50 mM Tris pH 7.4, 5 mM KCl, 20 mM $MgCl_2$, 1

450   mM EDTA, 0.5 mM TCEP, and 0.01% Triton. Proteins were pre-incubated in a 96-well plate

451   (Costar 3694) for 10 minutes at 37 °C before initiating the reaction by supplementing the ATP

452   regeneration mixture (5 mM ATP, 30 mM creatine phosphate, and 50 µg/mL creatine

453   phosphokinase). Fluorescence signal was monitored using a TECAN safire2 plate reader at 540

454   nm excitation and 580 nm emission wavelengths with 30 seconds intervals for 60 min. Each

455   reaction condition was repeated three times. Background fluorescence was measured by mixing

456   the same amount of substrate with 6 M guanidine-HCl and was subtracted from the average of

457   the experimental groups. Normalized fluorescence was plotted using GraphPad Prism 8.4.2.

458

459   **DATA AVAILABILITY**

460   Cryo-EM maps have been deposited in the Electron Microscopy Data Bank (EMDB)

461   under the accession codes EMDB-23449 (p97-Npl4/Ufd1-Ub$_n$-Eos-CHAPSO, Class 1), EMDB-

462   23450 (p97-Npl4/Ufd1-Ub$_n$-Eos-CHAPSO, Class 2), EMDB-23451 (p97-Npl4/Ufd1-Ub$_n$-Eos-

463   CHAPSO, Class 3), EMDB-23446 (p97-Npl4/Ufd1-Ub$_n$-Eos-FOM, Class 1), EMDB-23447 (p97-

464   Npl4/Ufd1-Ub$_n$-Eos-FOM, Class 2), EMDB-23448 (p97-Npl4/Ufd1-Ub$_n$-Eos-FOM, Class 3),

465   EMDB-23443 (p97-Npl4/Ufd1-Ub$_6$ -FOM, Class 1), EMDB-23444 (p97-Npl4/Ufd1-Ub$_6$-FOM,

466   Class 2), EMDB-23445 (p97-Npl4/Ufd1-Ub$_6$-FOM, Class 3), EMDB-23442 (p97-Npl4/Ufd1-Ub$_6$-

467   NMS-873-FOM), EMDB-23452 (p97-Npl4/Ufd1-Ub$_n$-Eos-NMS-873-CHAPSO), EMDB-23453

468   (p97-Npl4/Ufd1-Ub$_n$-Eos-NMS-873(substoichiometric)-CHAPSO, Class 1), EMDB-23454 (p97-

469   Npl4/Ufd1-Ub$_n$-Eos-NMS-873(substoichiometric)-CHAPSO, Class 2), EMDB-23455 (p97-

470   Npl4/Ufd1-Ub$_n$-Eos-NMS-873(substoichiometric)-CHAPSO, Class 3), EMDB-23456 (p97-

471   Npl4/Ufd1-Ub$_n$-Eos-NMS-873(substoichiometric)-CHAPSO, Class 4), EMDB-23457 (p97-

472   Npl4/Ufd1-Ub$_n$-Eos-NMS-873(substoichiometric)-CHAPSO, Class 5), EMDB-23458 (p97-

473   Npl4/Ufd1-Ub$_n$-Eos-NMS-873(substoichiometric)-CHAPSO, Class 6). The atomic models have

474   been deposited in the Protein Data Bank (PDB) under the accession codes 7LN5 (p97-

475   Npl4/Ufd1-Ub$_n$-Eos-CHAPSO, Class 1), 7LN6 (p97-Npl4/Ufd1-Ub$_n$-Eos-CHAPSO, Class 2),

476   7LN2 (p97-Npl4/Ufd1-Ub$_n$-Eos-FOM, Class 1), 7LN3 (p97-Npl4/Ufd1-Ub$_n$-Eos-FOM, Class 2),

477   7LN4 (p97-Npl4/Ufd1-Ub$_n$-Eos-FOM, Class 3), 7LMZ (p97-Npl4/Ufd1-Ub$_6$ -FOM, Class 1), 7LN0

478   (p97-Npl4/Ufd1-Ub$_6$-FOM, Class 2), 7LN1 (p97-Npl4/Ufd1-Ub$_6$-FOM, Class 3), 7LMY (p97-

479   Npl4/Ufd1-Ub$_6$-NMS-873-FOM).

480

481   **ACKNOWLEGEMENT**

490

491   **AUTHOR CONTRIBUTIONS**

492   M.P. and M.Z. designed all the experiments and interpreted the results. M.P., Y.Y., H.A.,

493   Q.Z., and Y.X. cloned, expressed, and purified all the complexes and carried out related

494   biochemical characterizations. M.P., Y.Y., and M.Z. performed cryo-EM data collection and

495   processing. M.Z., M.P., and L.L. wrote the paper. M.Z., L.L., and M.P. supervised the project.

496

497   **COMPETING INTERESTS**

498   The authors declare no competing interests.
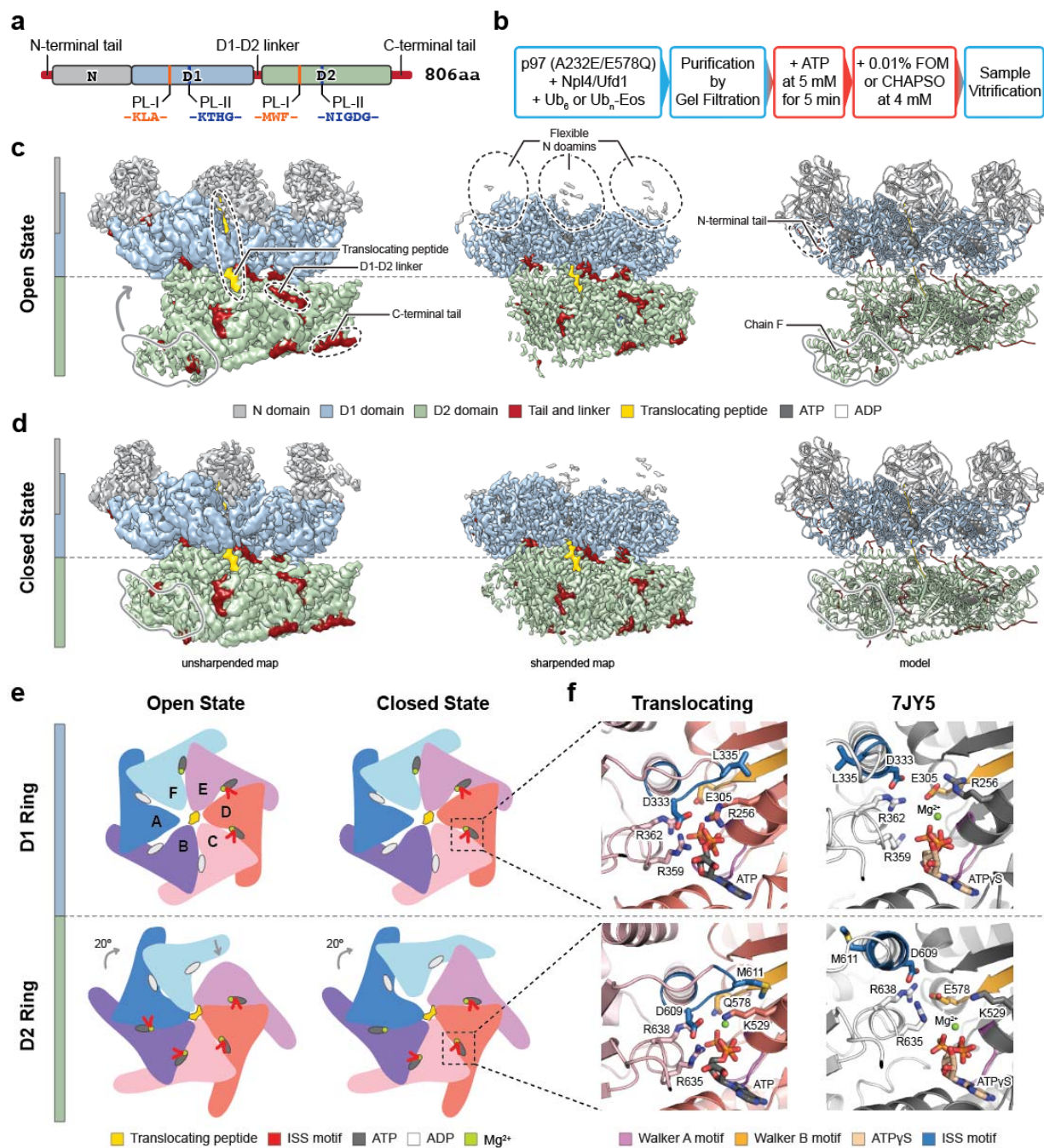
499

500

501

502

503

504

505 **FIGURE LEGENDS**

506 **FIGURE 1**

507

508

509

510

511 **Figure 1: Structures of human p97 in working states.**

512 **a,** Domain architecture of human p97. The color code of individual domains is used whenever

513 possible. Pore loop residues in D1 and D2 domains are listed. **b,** Sample preparation

514 procedures. Steps performed at 4 °C are in blue boxes. Steps performed at room temperature

515 are in red boxes. **c and d,** Cryo-EM maps and models of human p97 engaged with a

516 translocating peptide. The maps and models are aligned. Contour level: unsharpened map,

517 0.015; sharpened map, 0.035. **c,** Open state. **d,** Closed state. **e,** Illustrations showing the

518 arrangement of the D1 and D2 rings in the open and closed states, respectively. **f,** Magnified

519 views of compressed ATP binding sites in the D1 and D2 rings. The corresponding ATPγS

520 binding sites from the nontranslocating structure (PDB ID: 7JY5) are shown for comparison.

521

522   **FIGURE 2**
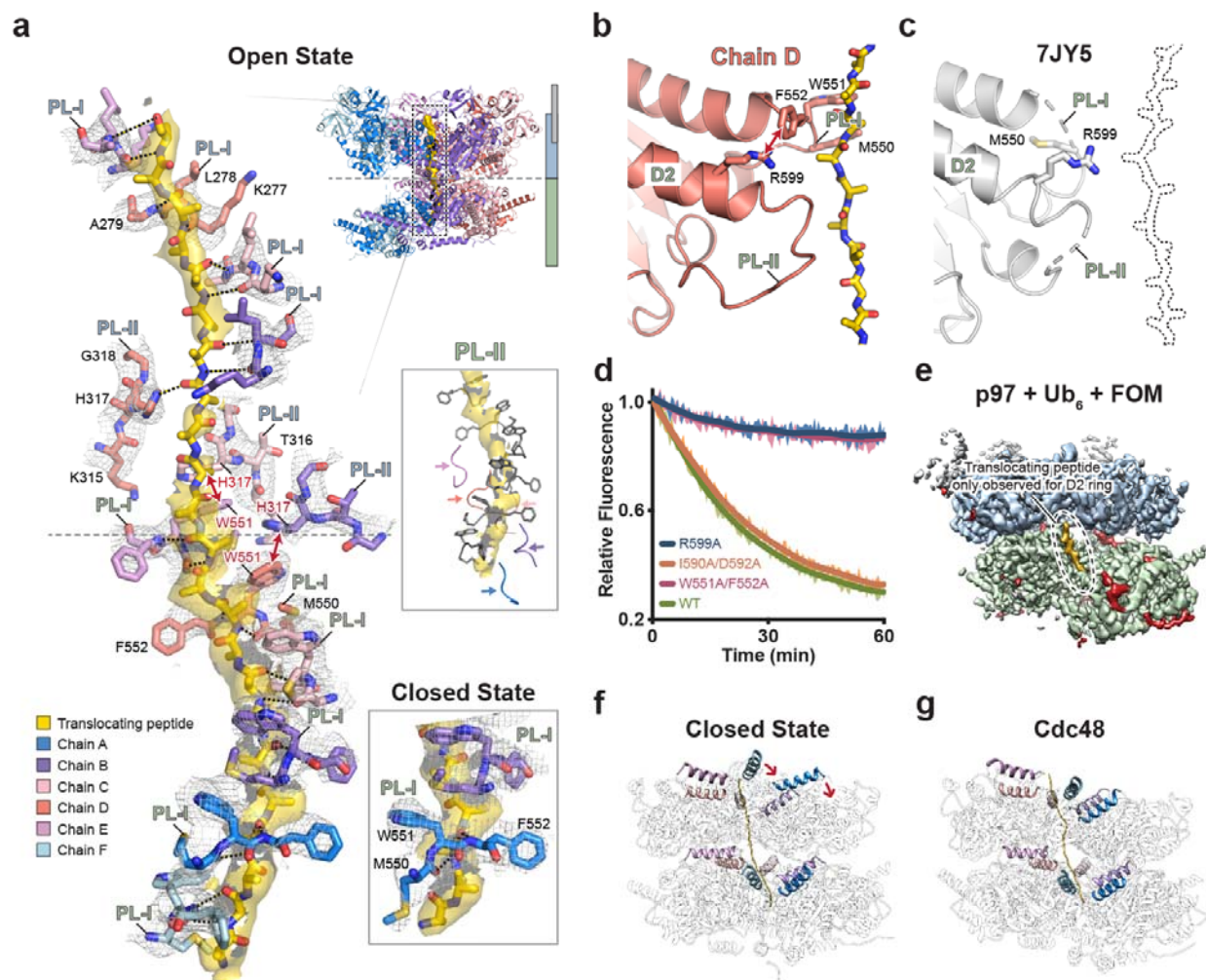
523

524   **Figure 2: Interactions between the pore loops and the substrate.**

525   **a,** Interactions between the translocating peptide and the interacting pore loops in the D1 and

526   D2 rings. The density of the pore loops and the translocating peptide are shown as a gray mesh

527   and yellow surface, respectively. Contour level: 6.0 root-mean-square deviation (rmsd). The

528   closed state and PL-II of the D2 ring are shown in the insets. Hydrogen bonds between the pore

529   loops and the peptide are labeled with black dotted lines. π-π interactions between H317 and

530   W551 are labeled with red double arrows. **b and c,** A comparison of the D2 domain in chain D

531   of the open state (panel **b**) and that of the nontranslocating structure (panel **c**, PDB ID: 7JY5).

532   The D2 domains are aligned. **d,** Substrate unfolding assay for the pore loop mutants of p97. The

533   error bands represent the standard deviation from triplicate experiments. **e,** Unsharpened cryo-

534   EM map (class 1) of the p97-Npl4/Ufd1-Ub$_6$-FOM dataset (**Extended Data Fig. 4**). The map is

535   shown in a similar orientation to **Fig. 1c and 1d**. Contour level: 0.015. **f and g**, A comparison of

536   cryo-EM models of translocating structures of p97 (closed state, panel **f**) and Cdc48 (PDB ID:

537   6OPC, panel **g**). The two models are aligned based on the D2 ring. The 2 helices immediately

538   before PL-I in D1 and D2 domains are colored. The color code is the same as that in panel **a**.

539

540   **FIGURE 3**
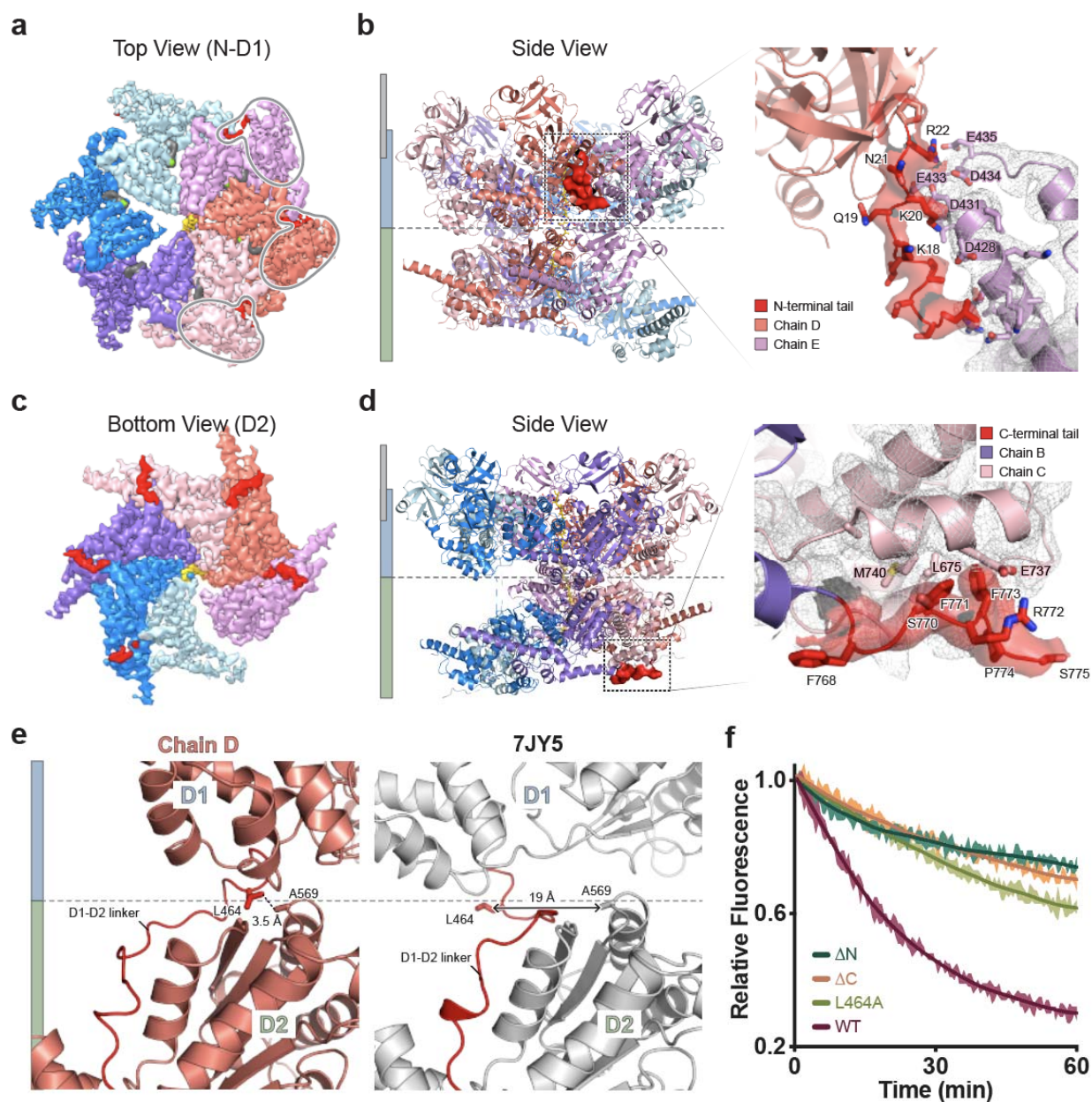
541

542

543   **Figure 3: N- and C-terminal tails and the linker between the D1 and D2 rings.**

544   **a,** Top view of the unsharpened cryo-EM map focused on the N and D1 domains (open state).

545   N-terminal tails are colored in red. Contour level: 0.015. **b,** A side view of the cryo-EM model of

546   the open state with the density of one N-terminal tail highlighted and magnified. Contour level:

547   6.0 rmsd. **c,** A bottom view of the unsharpened cryo-EM map focused on the D2 ring (open

548   state). C-terminal tails are shown in red. Contour level: 0.015. **d,** A side view of the cryo-EM

549   model of the open state with the density of one C-terminal tail highlighted and magnified.

550   Contour level: 6.0 rmsd. **e,** A comparison of the D1-D2 linker in chain D of the open state and

551   that of the nontranslocating structure (PDB ID: 7JY5). The D2 domains are aligned. **f,** Substrate

552   unfolding assay for tail and linker mutants of p97. The error bands represent the standard

553   deviation from triplicate experiments.

554

555   **FIGURE 4**
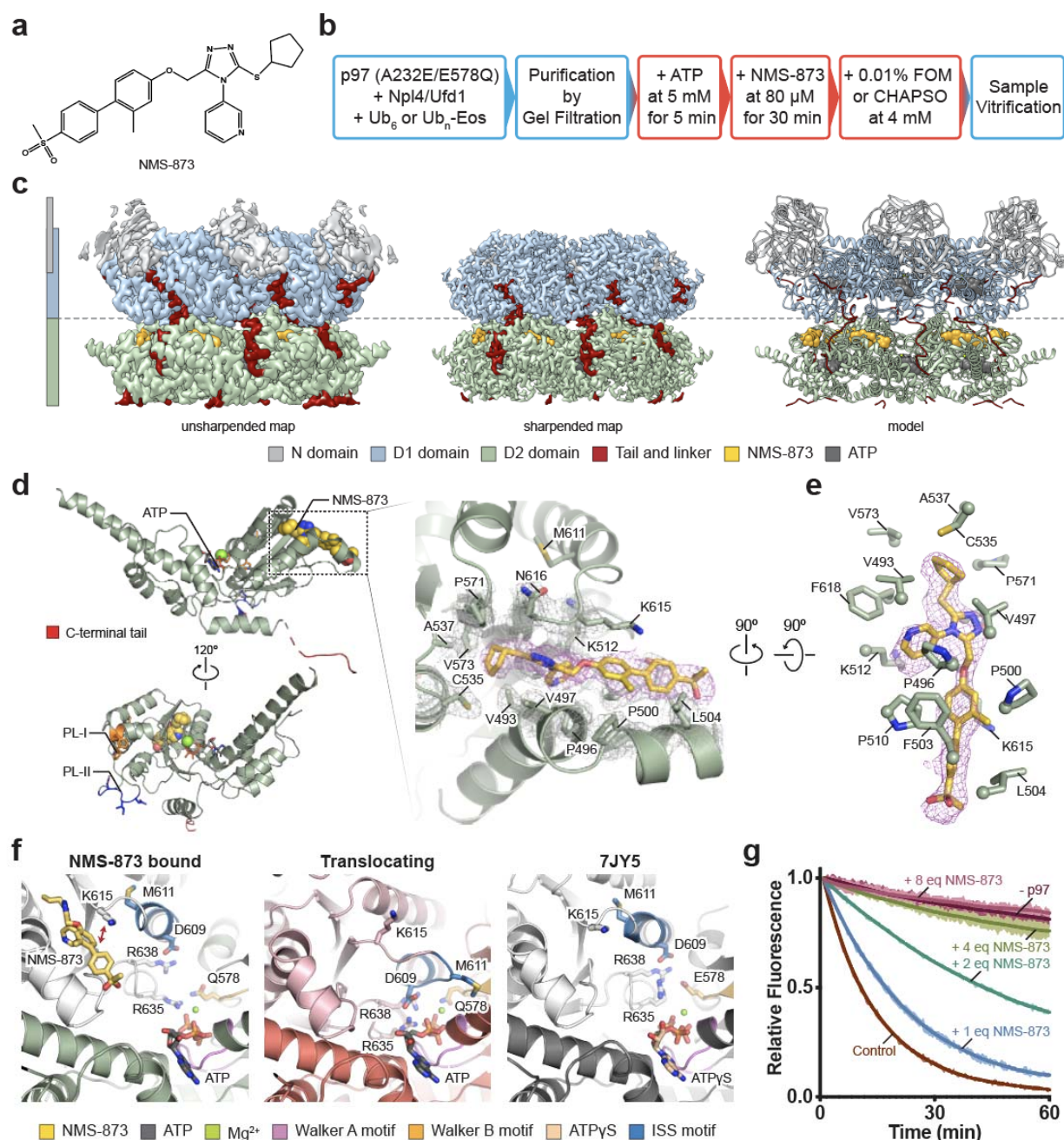
556

557   **Figure 4: NMS-873 inhibits translocation by locking the ISS motif.**
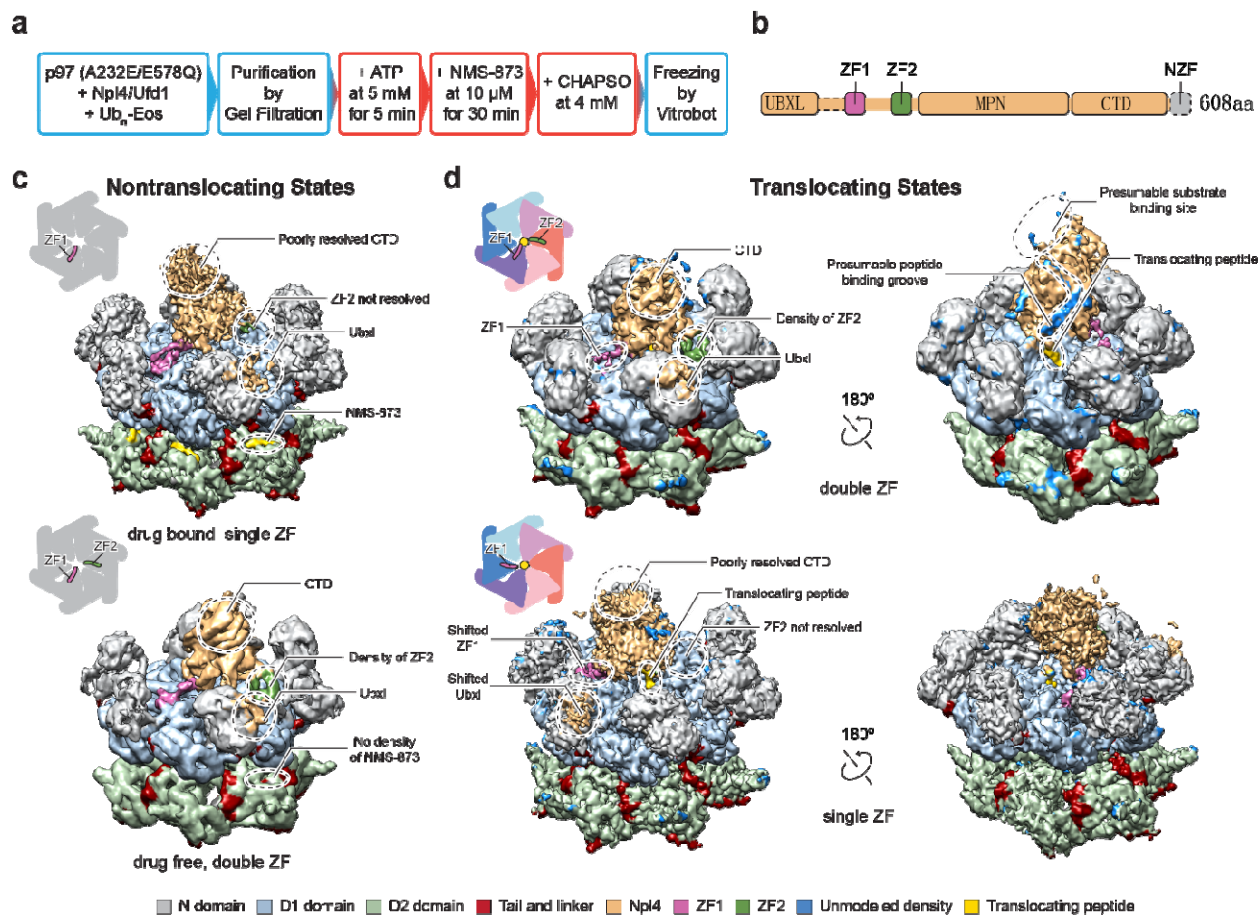
558   **a,** Chemical structure of NMS-873. **b,** Sample preparation procedures. Steps performed at 4 °C

559   are in blue boxes. Steps performed at room temperature are in red boxes. **c,** Cryo-EM maps

560   and models of human p97 in complex with NMS-873. The maps and models are aligned.

561   Contour level: unsharpened map, 0.018; sharpened map, 0.052. **d,** D2 domain of the complex

562   structure in panel **c**, with the NMS-873 binding site zoomed in. The density of NMS-873 and the

563   interacting residues are shown as magenta and gray mesh, respectively. Contour level: 6.0

564   rmsd. **e,** A different view of the NMS-873 binding site, with side chains of interacting residues

565   shown. Contour level: 6.0 rmsd. **f,** A comparison of nucleotide binding sites in NMS-873 bound,

566   translocating (chain D in open state), and nontranslocating (PDB ID: 7JY5) structures. The

567   bottom D2 domains (green, salmon, and gray) are aligned. **g,** Substrate unfolding assay for

568   wild-type p97 in the presence of different concentrations of NMS-873. One p97 hexamer can

569   bind 6 equivalents (eq) of NMS-873.

570

FIGURE 5

Figure 5: Conformational states of Npl4 in the presence of NMS873 at a substoichiometric concentration.

a, Sample preparation procedures. Steps performed at 4 °C are in blue boxes. Steps performed at room temperature are in red boxes. **b,** Domain architecture of human Npl4. The color code of the individual motifs are the same as that in panels **c** and **d**. Dotted parts are not resolved in the cryo-EM maps. **c,** Two cryo-EM maps in nontranslocating states resolved from the dataset (**Extended Data Fig. 10**), one bound with NMS-873 (top). **d,** Two cryo-EM maps in translocating states resolved from the dataset. Different positions of zinc finger motifs of Npl4 are illustrated in the insets.

583 **EXTENDED DATA FIGURES**

584 **EXTENDED DATA FIGURE 1**
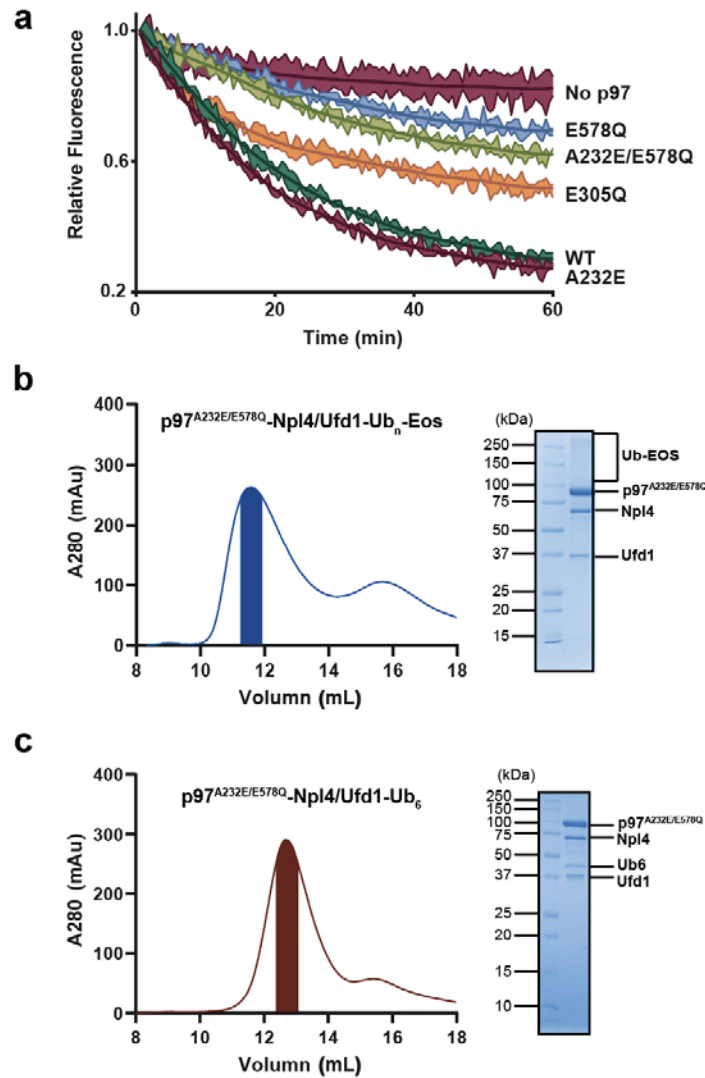
585

586 **Extended Data Figure 1: Substrate unfolding activity of various p97 mutants and the**

587 **purification of cofactor- and substrate-engaged p97 complexes.**

588 **a,** Substrate unfolding assay for wild-type (WT) p97 and various mutations. E305Q and E578Q

589 are the two Walker B mutations in the D1 and D2 domains, respectively. A232E is a disease

590 mutation found in multisystem proteinopathy (MSP)[27,31]. **b,** Gel filtration chromatogram and

591 SDS-PAGE gel of the p97$^{A232E/E578Q}$-Npl4/Ufd1-Ub$_n$-Eos complex. **c,** Gel filtration chromatogram

592 and SDS-PAGE gel of the p97$^{A232E/E578Q}$-Npl4/Ufd1-Ub$_n$-Eos complex.

593 **EXTENDED DATA FIGURE 2**

a

594

595   **Extended Data Figure 2: Single-particle cryo-EM analyses for the p97-Npl4/Ufd1-Ub$_n$-Eos-**

596   **CHAPSO dataset.**

597   **a,** The workflow of data processing. The dataset was subjected to particle selection, 2D

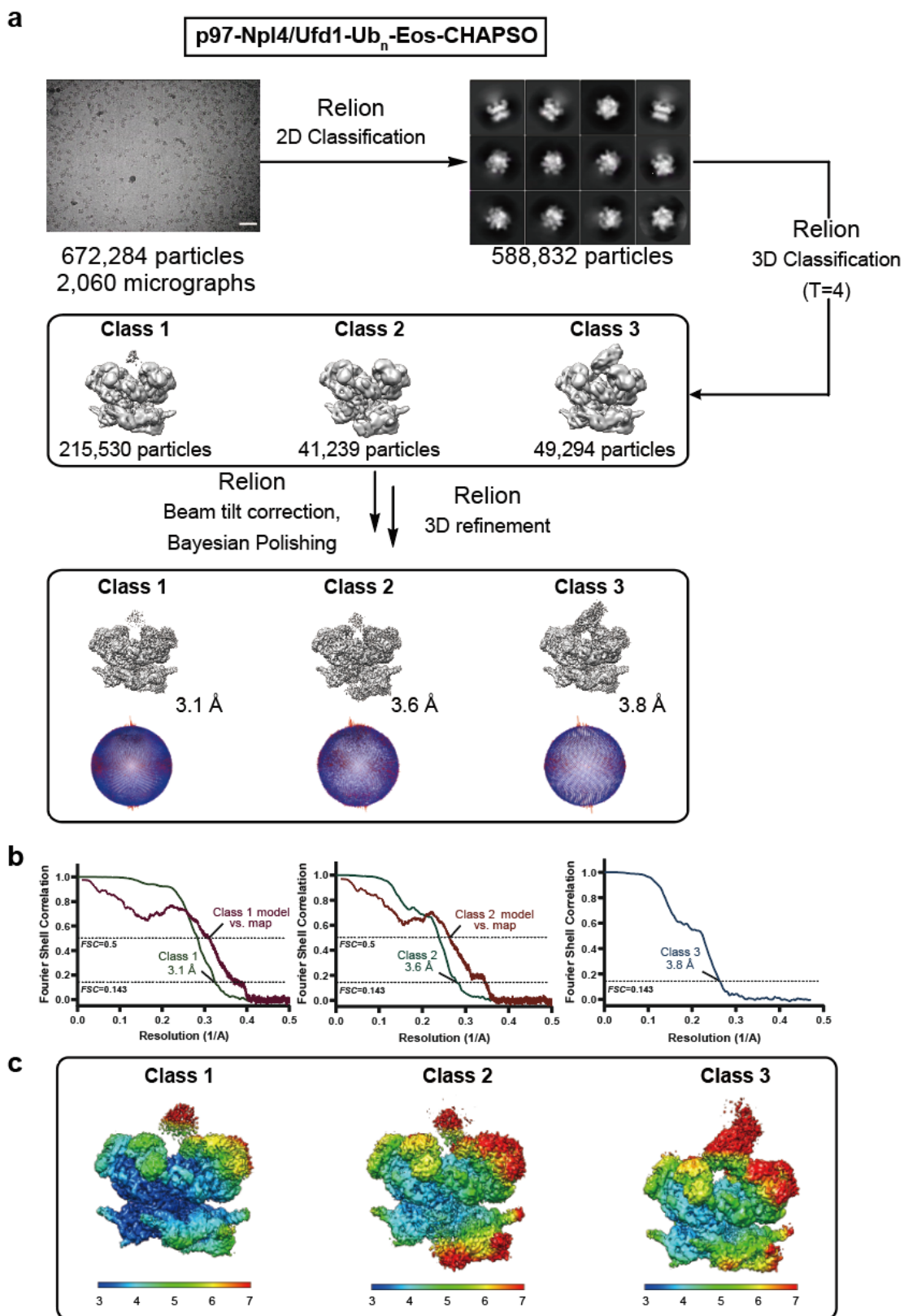598   classification, and multiple rounds of 3D classification. A representative micrograph (scale bar

599   corresponds to 50 nm) and representative 2D class averages are shown. Three classes were

600   resolved from the dataset, including class 1 (closed state), class 2 (open state), and class 3

601   (similar to the closed state but with the Npl4 density). The distributions of the Euler angles for

602   each reconstruction are shown below the maps. **b,** Fourier shell correlation (FSC) curves of the

603   masked maps after Relion postprocessing. The resolutions were determined by the FSC=0.143

604   criterion. The model vs. map FSC curves are also shown for class 1 and class 2 (red). **c,** Local

605   resolutions of the maps calculated using Relion.

606

607 **EXTENDED DATA FIGURE 3**

a

p97-Npl4/Ufd1-Ub$_n$-Eos-FOM

Relion
2D Classification

2,845,403 particles
5,235 micrographs

2,697,259 particles

Relion
3D Classification
(T=4)

Class 1   Class 2   Class 3

72,646 particles   256,471 particles   723,840 particles

Relion
Beam tilt correction,
Bayesian Polishing

Relion
3D refinement

Class 1   Class 2   Class 3

3.6 Å   3.4 Å   3.0 Å

b

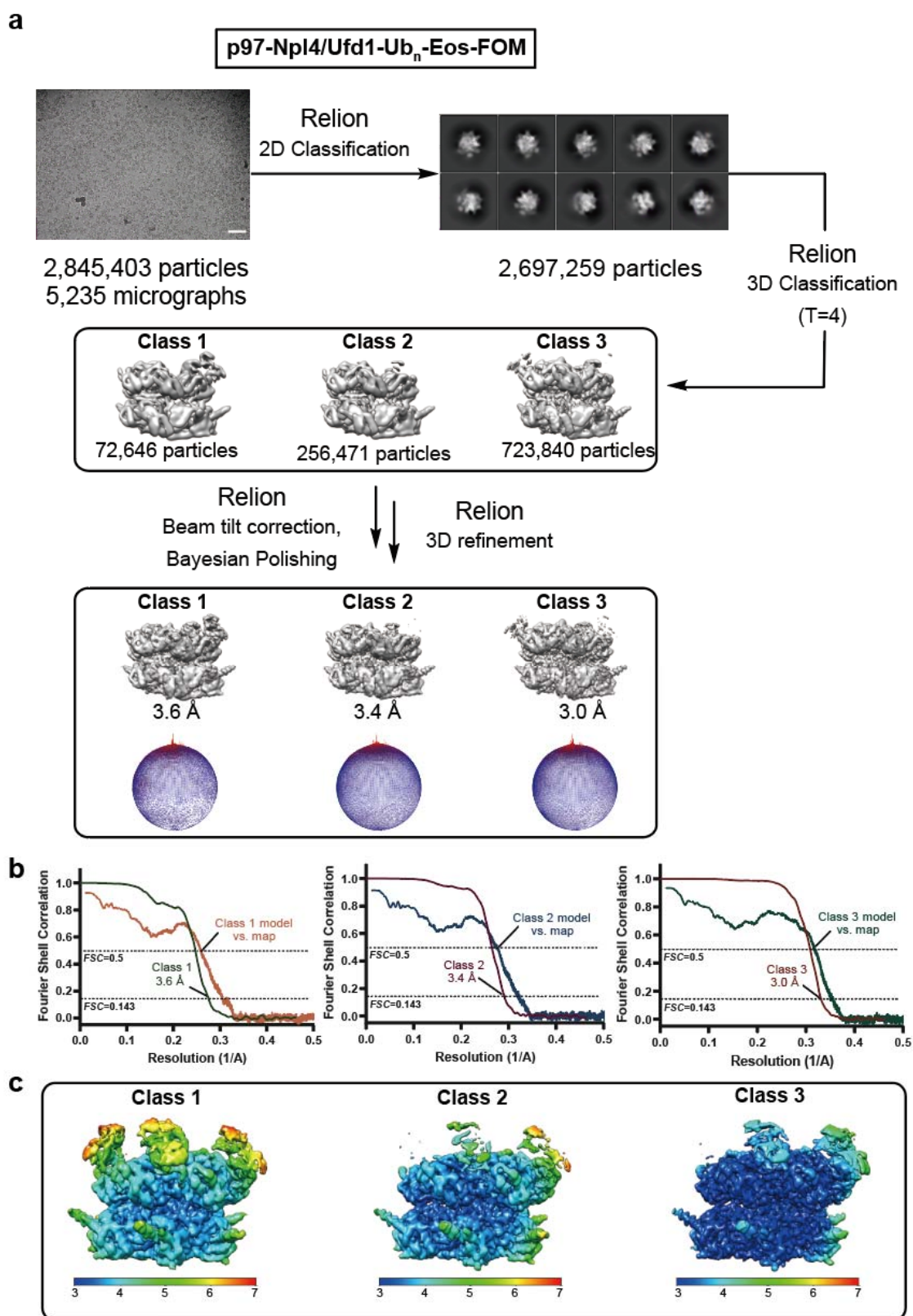

c

Class 1   Class 2   Class 3

608

609 **Extended Data Figure 3: Single-particle cryo-EM analyses for the p97-Npl4/Ufd1-Ub$_n$-Eos-**

610 **FOM dataset.**

611 **a,** The workflow of data processing. The dataset was subjected to particle selection, 2D

612 classification, and multiple rounds of 3D classification. A representative micrograph (scale bar

613 corresponds to 50 nm) and representative 2D class averages are shown. Three classes were

614 resolved from the dataset. The distributions of the Euler angles for each reconstruction are

615 shown below the maps. **b,** FSC curves of the masked maps after Relion postprocessing. The

616 resolutions were determined by the FSC=0.143 criterion. The model vs. map FSC curves for

617 each class are also shown. **c,** Local resolutions of the maps calculated using Relion.
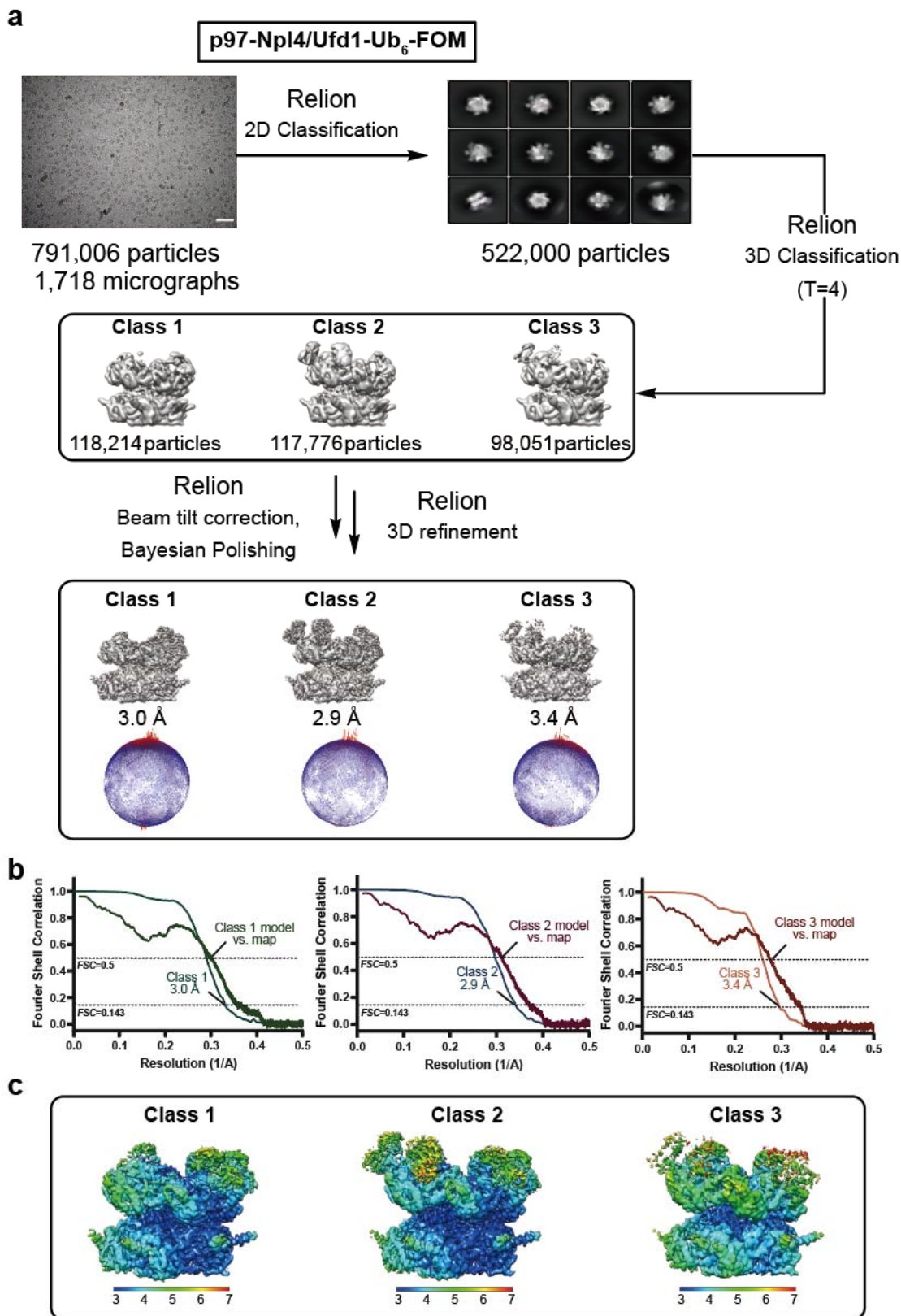
618

619 **EXTENDED DATA FIGURE 4**

620

621 **Extended Data Figure 4: Single-particle cryo-EM analyses for the p97-Npl4/Ufd1-Ub$_6$-FOM**

622 **dataset.**

623 **a,** The workflow of data processing. The dataset was subjected to particle selection, 2D

624 classification, and multiple rounds of 3D classification. A representative micrograph (scale bar

625 corresponds to 50 nm) and representative 2D class averages are shown. Three classes were

626 resolved from the dataset. The distributions of the Euler angles for each reconstruction are

627 shown below the maps. **b,** FSC curves of the masked maps after Relion postprocessing. The

628 resolutions were determined by the FSC=0.143 criterion. The model vs. map FSC curves for

629 each class are also shown. **c,** Local resolutions of the maps calculated using Relion.

630

631

632   **EXTENDED DATA FIGURE 5**
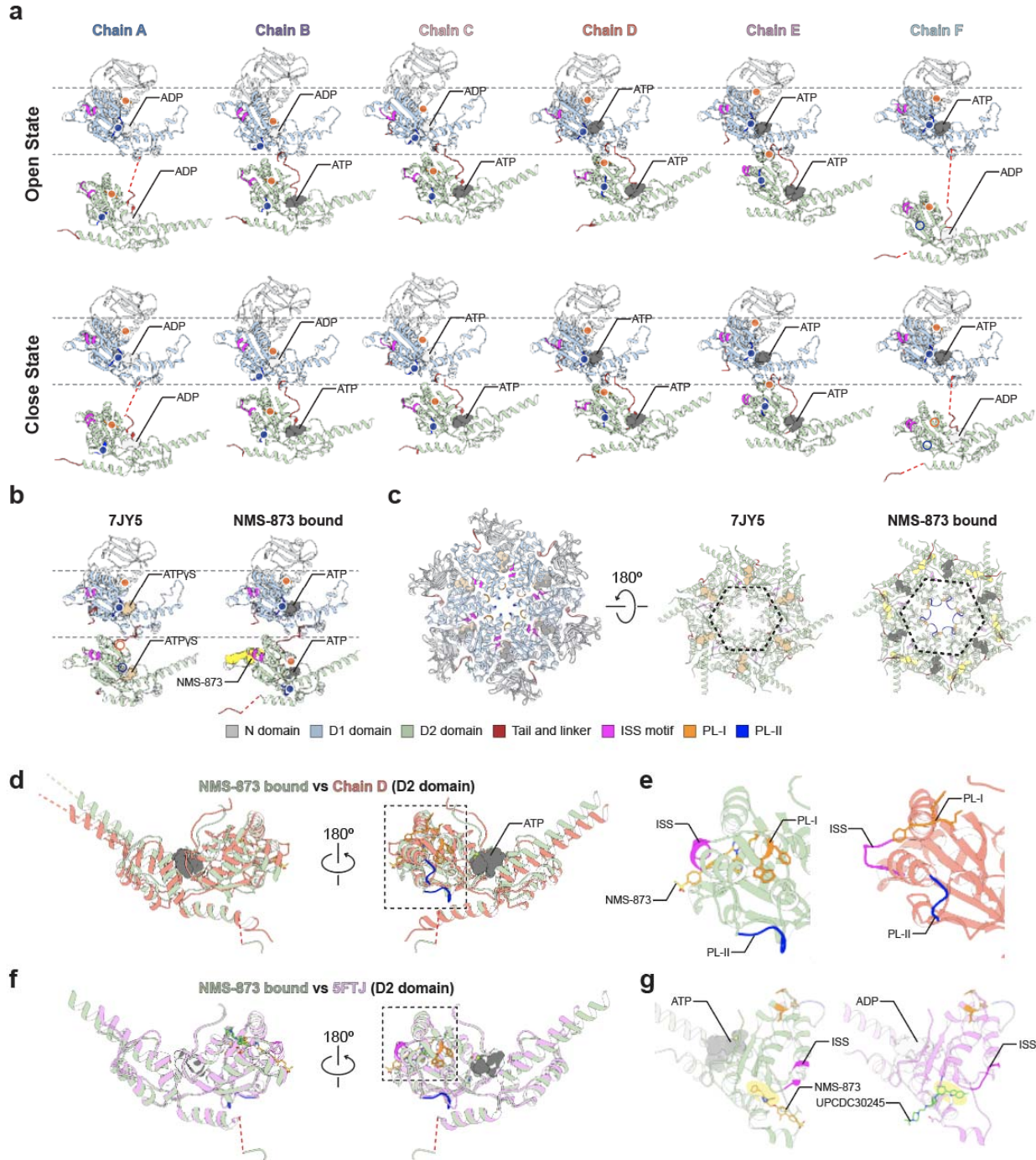
633

634   **Extended Data Figure 5: Comparison of various p97 structures.**

635   **a,** Unrolling of the open (top row) and closed (bottom row) states of p97. The lateral and vertical

636   movement of D2 domains can be visualized. The positions of pore loops are marked with solid

637   dots. Unresolved pore loops are marked by open circles. **b,** Unrolling of the ATPγS-bound

638   nontranslocating structure (PDB ID: 7JY5) and NMS-873-bound structure. Only one chain of

639   each structure is shown since both structures are sixfold symmetric. **c,** A superimposition of

640   7JY5- and NMS-873-bound structures. Left: a top view of the N and D1 domains; Right: a

641   bottom view of the D2 ring. The opening of the D2 ring is marked by a dotted hexagon. Panels **a,**

642   **b,** and **c** share the same color code. **d,** A comparison of the D2 domain in the NMS-873-bound

643   structure and that in chain D of the open state. The superimposition is based on the α/β

644   subdomain. **e,** Magnified views of the dotted box in panel **d**, showing the conformations of the

645   PL-I, PL-II, and ISS motifs. **f,** A comparison of the D2 domain in NMS-873- and UPCDC30245

646   (PDB ID: 5FTJ)-bound structures. The superimposition is based on the α/β subdomain. **g,**

647   Magnified views of the dotted box in panel **f**, showing the binding sites of the compounds and

648   the conformations of the ISS motif.

649

650 **EXTENDED DATA FIGURE 6**
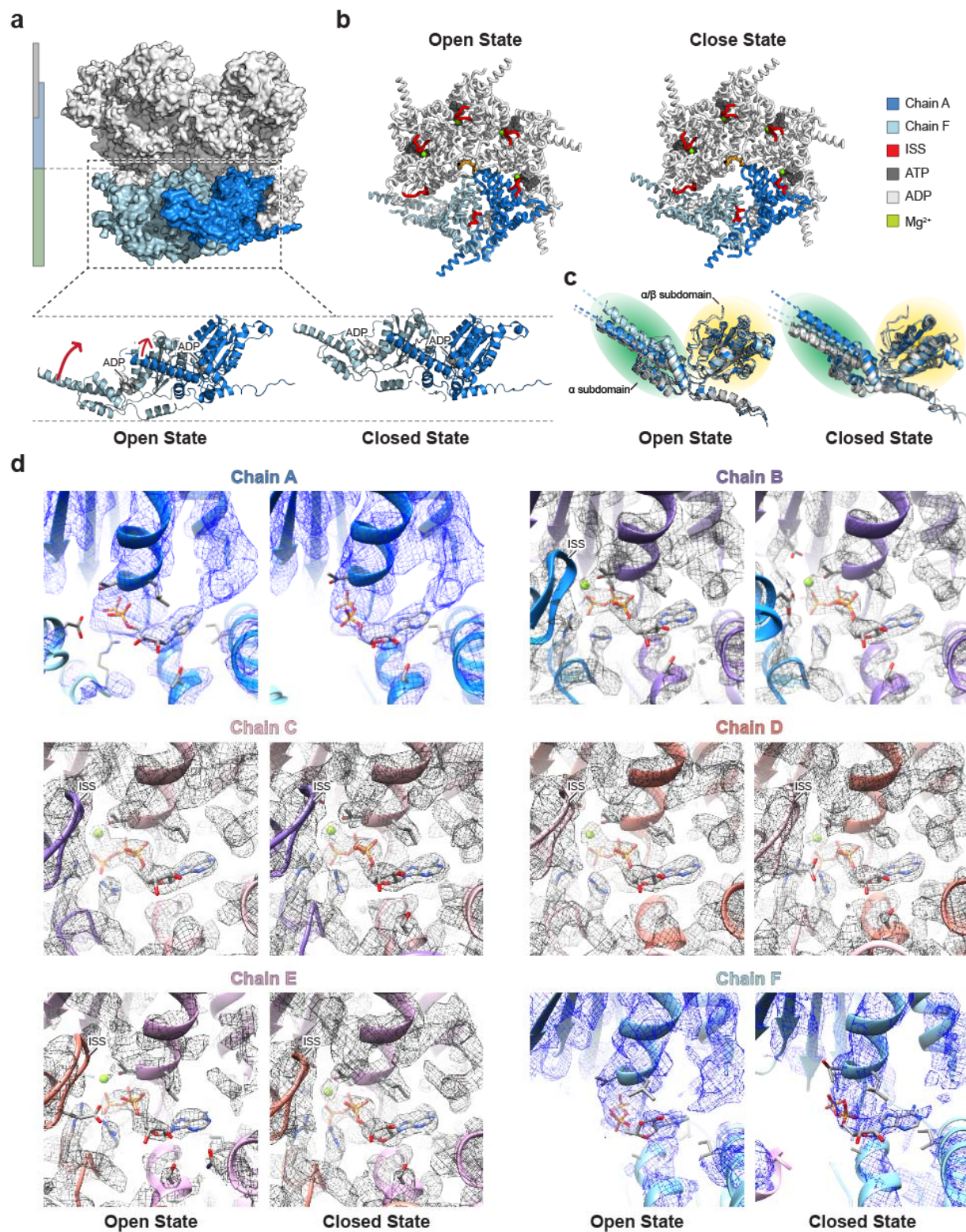
651

652 **Extended Data Figure 6: The power stroke motion and the nucleotide binding sites of the**

653 **D2 domains.**

654 **a,** A superimposition of the open and closed state structures, with two D2 domains (chain A and

655 chain F) magnified. The relative positions of the D2 domains in chain A and chain F can be

656 visualized. **b,** Top views of the D2 ring in the open and closed states, highlighting chain A, chain

657 F, and the ISS motifs. **c,** Superimpositions of all D2 domains in the open and closed states

658 based on the α/β subdomain. The directions of α7 helices are highlighted by dotted lines for

659 comparison (dark blue, chain A; light blue, chain F; and gray, other chains). **d,** Individual

660 nucleotide binding sites of the D2 domains in the open and closed states. Blue mesh:

661 unsharpened map at contour level; Gray mesh: sharpened map at contour level.;
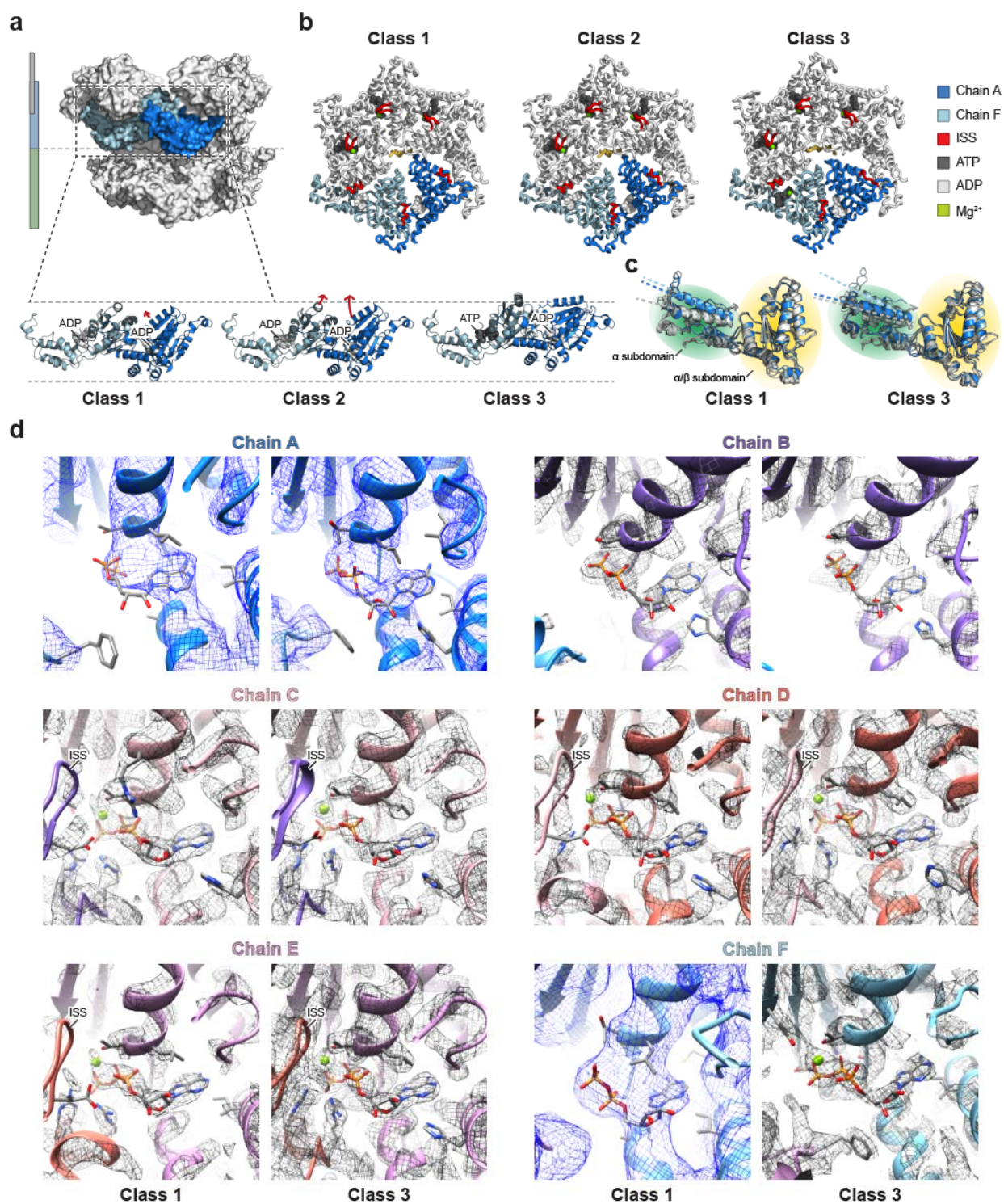
662

663 **EXTENDED DATA FIGURE 7**

664

665

666 **Extended Data Figure 7: The power stroke motion and the nucleotide binding sites of the**

667 **D1 domains.**

668 **a,** A superimposition of three structures (classes 1, 2, and 3) from the p97-Npl4/Ufd1-Ub$_n$-Eos-

669 FOM dataset, with two D1 domains (chain A and chain F) magnified. The relative positions of

670 the D1 domains in chain A and chain F can be visualized. **b,** Top views of the D1 ring in the

671 three classes, highlighting chain A, chain F, and the ISS motifs. **c,** Superimpositions of all D1

672 domains in class 1 and class 3 based on the α/β subdomain. The directions of α7 helices are

673 highlighted by dotted lines for comparison (dark blue, chain A; light blue, chain F; and gray,

674 other chains). **d,** Individual nucleotide binding sites of the D1 domains in class 1 and class 3.

675 Blue mesh: Unsharpened map at contour level; Gray mesh: sharpened map at contour level.;
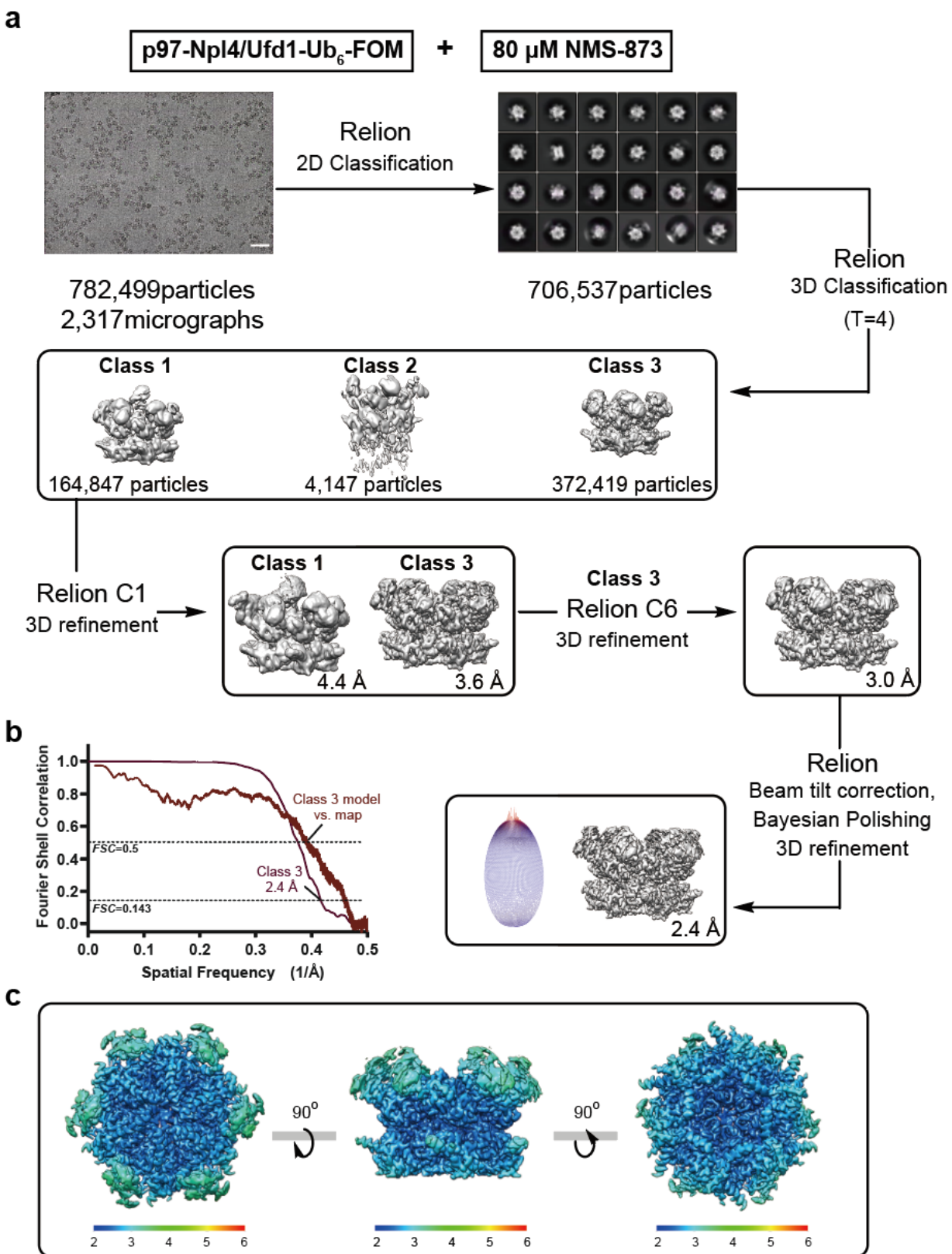
676

677 **EXTENDED DATA FIGURE 8**

678

679 **Extended Data Figure 8: Single-particle cryo-EM analyses for the p97-Npl4/Ufd1-Ub$_6$**

680 **complex in the presence of 80 μM NMS-873.**

681 **a,** The workflow of data processing. The dataset was subjected to particle selection, 2D

682 classification, and multiple rounds of 3D classification. A representative micrograph (scale bar

683 corresponds to 50 nm) and representative 2D class averages are shown. A single class was

684 resolved from the dataset. The distribution of the Euler angles is shown next to the map. **b,** The

685 FSC curve of the masked map after Relion postprocessing. The resolution was determined by

686 the FSC=0.143 criterion. The model vs. map FSC curve is also shown. **c,** Local resolution of the

687 map calculated using Relion.

688

689

690 **EXTENDED DATA FIGURE 9**

692   **Extended Data Figure 9: Single-particle cryo-EM analyses for the p97-Npl4/Ufd1-Ub$_n$-Eos**

693   **complex in the presence of 80 μM NMS-873.**

694   **a,** The workflow of data processing. The dataset was subjected to particle selection, 2D

695   classification, and multiple rounds of 3D classification. A representative micrograph (scale bar

696   corresponds to 50 nm) and representative 2D class averages are shown. A single class was

697   resolved from the dataset. The distribution of the Euler angles is shown next to the map. **b,** The

698   FSC curve of the masked map after Relion postprocessing. The resolution was determined by

699   the FSC=0.143 criterion. **c,** Local resolution of the map calculated using Relion.

700

701

702

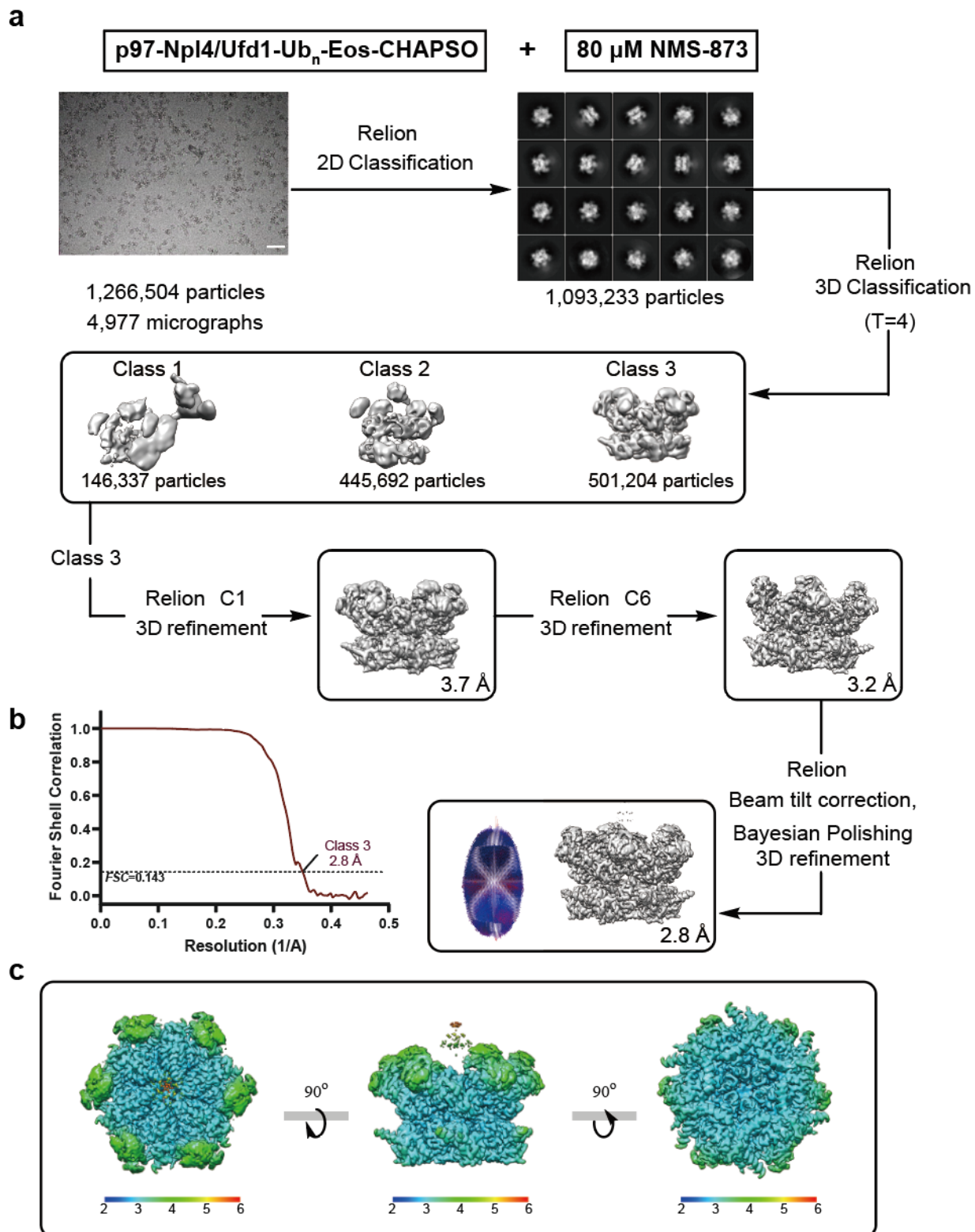703 **EXTENDED DATA FIGURE 10:**

704
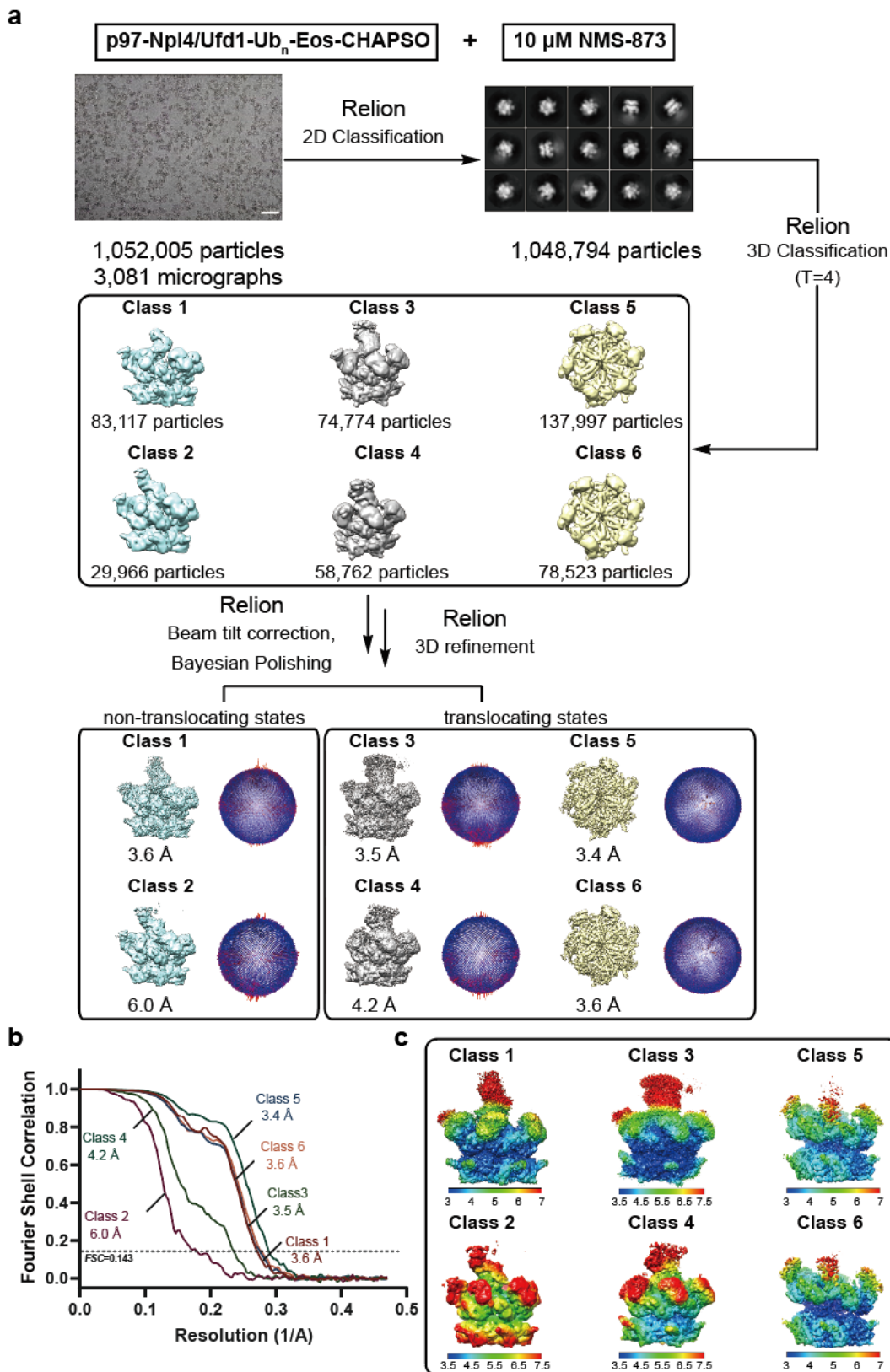
705 **Extended Data Figure 10: Single-particle cryo-EM analyses for the p97-Npl4/Ufd1-Ub$_n$-**

706 **Eos complex in the presence of 10 μM NMS-873.**

707 **a,** The workflow of data processing. The dataset was subjected to particle selection, 2D

708 classification, and multiple rounds of 3D classification. A representative micrograph (scale bar

709 corresponds to 50 nm) and representative 2D class averages are shown. Six classes were

710 resolved from the dataset, including two in nontranslocating states (Class 1 and Class 2) and

711 four in translocating states (Class 3 through Class 6). The distributions of the Euler angles for

712 each reconstruction are shown next to the maps. **b,** FSC curves of the masked maps after

713 Relion postprocessing. The resolutions were determined by the FSC=0.143 criterion. **c,** Local

714 resolutions of the maps calculated using Relion.

715

716

717

718

719 **EXTENDED DATA TABLE 1: Statistics of cryo-EM data collection and processing**

	p97-Npl4/Ufd1-Ub$_n$-Eos			p97-Npl4/Ufd1-Ub$_n$-Eos		
Detergent	CHAPSO (4 mM)			FOM (0.001%)		
Microscope	Krios (UChicago)			Krios (NCI)		
Magnification	81,000			81,000		
Voltage (kV)	300			300		
Spherical aberration (mm)	2.7			2.7		
Detector	K3			K3		
Camera mode	Super resolution counting			Super resolution counting		
Exposure rate (e$^-$/pixel/s)	15			15		
Total exposure (e$^-$/Å^2)	50			50		
Defocus range (μm)	-1.0 to -2.5			-1.0 to -2.5		
Pixel size (Å)	1.063			1.0794		
Mode of data collection	Image shift			Image shift		
Energy filter	20 eV slit			20 eV slit		
Software for data collection	EPU			Latitude S		
Number of micrographs	2,060			5,235		
Symmetry imposed	C1			C1		
Box size (pixel)	320			320		
Initial particle images (no.)	672,284			2,845,403		
Particle images for 3D (no.)	588,832			2,697,259		
	Class 1	Class 2	Class 3	Class 1	Class 2	Class 3
Final particle images (no.)	215,530	41,239	49,294	72,646	256,471	723,840
Map resolution, masked (Å)	3.09	3.58	3.77	3.63	3.45	3.02
B-factor estimated (Å^2)	79.7	79.7	80.3	97.6	109	96.8
EMD accession code	23449	23450	23451	23446	23447	23448

720

	p97-Npl4/Ufd1-Ub$_6$		
Detergent	FOM (0.001%)		
Microscope	Krios (UChicago)		
Magnification	81,000		
Voltage (kV)	300		
Spherical aberration (mm)	2.7		
Detector	K3		
Camera mode	Super resolution counting		
Exposure rate (e$^-$/pixel/s)	15		
Total exposure (e$^-$/Å^2)	50		
Defocus range (μm)	-1.0 to -2.5		
Pixel size (Å)	1.063		
Mode of data collection	Image shift		
Energy filter	20 eV slit		
Software for data collection	EPU		
Number of micrographs	1,718		
Symmetry imposed	C1		
Box size (pixel)	320		
Initial particle images (no.)	791,006		
Particle images for 3D (no.)	522,000		
	Class 1	Class 2	Class 3
Final particle images (no.)	118,214	117,776	98,051
Map resolution, masked (Å)	3.06	2.98	3.40
B-factor estimated (Å^2)	69.1	64.7	77.3
EMD accession code	23443	23444	23445

721
722

	p97-Npl4/Ufd1-Ub$_6$-NMS-873 (80 μM)	p97-Npl4/Ufd1-Ub$_n$-Eos-NMS-873 (80 μM)
Detergent	FOM (0.001%)	CHAPSO (4 mM)
Microscope	Krios (UChicago)	Krios (NCI)
Magnification	81,000	81,000
Voltage (kV)	300	300
Spherical aberration (mm)	2.7	2.7
Detector	K3	K3
Camera mode	Super resolution counting	Super resolution counting
Exposure rate (e$^-$/pixel/s)	15	15
Total exposure (e$^-$/Å^2)	50	50
Defocus range (μm)	-1.0 to -2.5	-1.0 to -2.5
Pixel size (Å)	1.063	1.0794
Mode of data collection	Image shift	Image shift
Energy filter	20 eV slit	20 eV slit
Software for data collection	EPU	Latitude S
Number of micrographs	2,317	4,977
Symmetry imposed	C6	C6
Box size (pixel)	320	320
Initial particle images (no.)	782,499	1,266,504
Particle images for 3D (no.)	706,537	1,093,233
Final particle images (no.)	372,419	501,204
Map resolution, masked (Å)	2.41	2.87
B-factor estimated (Å^2)	58.8	96.2
EMD accession code	23442	23452

723
724

	p97-Npl4/Ufd1-Ub$_n$-Eos-NMS-873 (10 µM)					
Detergent	CHAPSO (4 mM)					
Microscope	Krios (UChicago)					
Magnification	81,000					
Voltage (kV)	300					
Spherical aberration (mm)	2.7					
Detector	K3					
Camera mode	Super resolution counting					
Exposure rate (e$^-$/pixel/s)	15					
Total exposure (e$^-$/Å^2)	50					
Defocus range (µm)	-1.0 to -2.5					
Pixel size (Å)	1.063					
Mode of data collection	Image shift					
Energy filter	20 eV slit					
Software for data collection	Latitude S					
Number of micrographs	3081					
Symmetry imposed	C1					
Box size (pixel)	320					
Initial particle images (no.)	1,052,005					
Particle images for 3D (no.)	1,048,794					
	Non-Translocating		Translocating			
	Class 1	Class 2	Class 3	Class 4	Class 5	Class 6
Final particle images (no.)	83,317	29,966	74,774	58,762	137,997	78,523
Map resolution, masked (Å)	3.69	6.07	3.58	4.25	3.47	3.65
B-factor estimated (Å^2)	105	198	93.0	129	91.7	92.0
EMD accession code	23453	23454	23455	23456	23457	23458

725
726

727 **EXTENDED DATA TABLE 2: Statistics of cryo-EM model refinement and geometry**
728

Dataset: p97-Npl4/Ufd1-Ub$_n$-Eos-CHAPSO		
	Class1 (Closed State)	**Class2 (Open State)**
Composition (#)		
Chains	8	8
Atoms	35,051	35,072
Residues	Protein: 4,447	Protein: 4,456
Water	0	0
Ligands	MG: 7	MG: 7
	ADP: 5	ADP: 5
	ATP: 7	ATP: 7
Bonds (RMSD)		
Length (Å)	0.003	0.004
Angles (°)	0.617	0.673
MolProbity score	1.52	1.68
Clash score	9.95	10.93
Ramachandran plot (%)		
Outliers	0.00	0.02
Allowed	1.54	2.63
Favored	98.46	97.35
Rotamer outliers (%)	0.03	0.03
Cβ outliers (%)	0.00	0.00
Peptide plane (%)		
Cis proline/general	10.1/0.0	10.2/0.0
Twisted proline/general	0.0/0.0	0.0/0.0
CaBLAM outliers (%)	1.83	1.58
ADP (B-factors)		
Iso/Aniso (#)	35,051/0	35072/0
min/max/mean		
Protein	0.48/75.21/37.58	0.36/49.31/19.03
Ligand	11.67/65.09/33.22	2.26/41.30/13.85
PDB accession code	7LN5	7LN6

729
730

Dataset: p97-Npl4/Ufd1-Ub$_n$-Eos-FOM			
	Class1	**Class2**	**Class3**
Composition (#)			
Chains	8	8	8
Atoms	34,941	34,920	35,103
Residues	Protein: 4,433	Protein: 4,431	Protein: 4,455
Water	0	0	0
Ligands	MG: 7	MG: 7	MG: 8
	ADP: 5	ADP: 5	ADP: 4
	ATP: 7	ATP: 7	ATP: 8
Bonds (RMSD)			
Length (Å)	0.004	0.005	0.003
Angles (°)	0.651	0.674	0.604
MolProbity score	1.57	1.55	1.43
Clash score	11.31	10.70	7.52
Ramachandran plot (%)			
Outliers	0.07	0.07	0.00
Allowed	1.61	1.75	2.07
Favored	98.32	98.18	97.93
Rotamer outliers (%)	0.00	0.00	0.03
Cβ outliers (%)	0.00	0.00	0.00
Peptide plane (%)			
Cis proline/general	8.5/0.0	8.5/0.0	10.1/0.0
Twisted proline/general	0.0/0.0	0.0/0.0	0.0/0.0
CaBLAM outliers (%)	1.58	1.65	1.48
ADP (B-factors)			
Iso/Aniso (#)	34,941/0	34,920/0	35,103/0
min/max/mean			
Protein	0.79/73.39/37.41	0.45/71.85/36.71	0.39/86.71/50.32
Ligand	7.76/90.54/36.11	7.16/72.98/34.80	15.72/92.31/44.90
PDB accession code	7LN2	7LN3	7LN4

731
732

Dataset: p97-Npl4/Ufd1-Ub$_6$-FOM			
	Class1	**Class2**	**Class3**
Composition (#)			
Chains	8	8	8
Atoms	34,994	34,983	34,796
Residues	Protein: 4,434	Protein: 4,434	Protein:
Water	0	0	0
Ligands	MG: 8	MG: 7	MG: 7
	ADP: 4	ADP: 4	ADP: 5
	ATP: 8	ATP: 8	ATP: 7
Bonds (RMSD)			
Length (Å)	0.004	0.003	0.006
Angles (°)	0.654	0.646	0.759
MolProbity score	1.60	1.59	1.79
Clash score	12.30	11.95	14.43
Ramachandran plot (%)			
Outliers	0.09	0.05	0.05
Allowed	1.64	1.75	2.63
Favored	98.27	98.20	97.32
Rotamer outliers (%)	0.00	0.03	0.00
Cβ outliers (%)	0.00	0.00	0.00
Peptide plane (%)			
Cis proline/general	8.9/0.0	8.9/0.0	9.0/0.0
Twisted proline/general	0.0/0.0	0.0/0.0	0.0/0.0
CaBLAM outliers (%)	1.60	1.67	
ADP (B-factors)			
Iso/Aniso (#)	34,994/0	34,983/0	34,796/0
min/max/mean			
Protein	3.48/79.40/39.29	2.27/77.11/40.21	2.28/70.59/33.60
Ligand	12.21/68.94/37.64	8.22/74.08/36.83	11.82/52.39/30.60
PDB accession code	7LMZ	7LN0	7LN1

733

Dataset: p97-Npl4/Ufd1-Ub$_6$-NMS-873 (80 μM)	
Composition (#)	
Chains	6
Atoms	35,646
Residues	Protein: 4,470
Water	0
Ligands	MG: 12
	NM3: 6 (NMS-873)
	ATP: 6
Bonds (RMSD)	
Length (Å)	0.003 (0)
Angles (°)	0.845 (3)
MolProbity score	1.79
Clash score	8.11
Ramachandran plot (%)	
Outliers	0.00
Allowed	2.71
Favored	97.29
Rotamer outliers (%)	1.89
Cβ outliers (%)	0.00
Peptide plane (%)	
Cis proline/general	10.0/0.0
Twisted proline/general	0.0/0.0
CaBLAM outliers (%)	0.95
ADP (B-factors)	
Iso/Aniso (#)	35,646/0
min/max/mean	
Protein	1.58/57.10/22.25
Ligand	2.92/28.45/15.85
PDB accession code	7LMY

734
735

736 **EXTENDED DATA TABLE 3: A summary of human p97 disease mutations and potentially**
737 **affected structures**
738

Disease Mutations	Potentially Affected Structures
R93C/R93H, I114V, I151V	N domain structure
I126F, T127A, P137L, M158V, R159G/R159C/R159H, E185K	N-cofactor interaction
I27V, R95C/R95G/R95H, G97E, R155S/R155H/R155L, G156C/G156S, G157R, M158V, R159G/R159C/R159H, R191G/R191Q, L198W, G202W, A232E, T262A, K386E, N387H/N387S/N387T, A439S/A439P/A439G	N-D1 interaction
I206F	D1 nucleotide binding site
A232E	D1-D1 interaction
D395G	D1 domain structure
N401S	D1-D2 interaction
R487H, R662C	D2-D2 interaction
D592N	Pore loop II of D2 domain
N750S	C terminal tail

739

REFERENCES

1   Bodnar, N. & Rapoport, T. Toward an understanding of the Cdc48/p97 ATPase. *F1000Res* **6**, 1318 (2017).

2   Erzberger, J. P. & Berger, J. M. Evolutionary relationships and structural mechanisms of AAA+ proteins. *Annu. Rev. Biophys. Biomol. Struct. 35, 93-114* (2006).

3   Rabouille, C., Levine, T. P., Peters, J.-M. & Warren, G. An NSF-like ATPase, p97, and NSF mediate cisternal regrowth from mitotic golgi fragments. *Cell* **82**, 905-914 (1995).

4   van den Boom, J. & Meyer, H. VCP/p97-Mediated Unfolding as a Principle in Protein Homeostasis and Signaling. *Mol Cell.* **69**, 182-194 (2018).

5   Ye, Y. H., Tang, W. K., Zhang, T. & Xia, D. A Mighty "Protein Extractor" of the Cell: Structure and Function of the p97/CDC48 ATPase. *Front Mol Biosci.* **4**, 39 (2017).

6   Tang, W. K. & Xia, D. Mutations in the Human AAA+ Chaperone p97 and Related Diseases. *Front Mol Biosci.* **3**, 79 (2016).

7   Darwich, N. F. *et al.* Autosomal dominant VCP hypomorph mutation impairs disaggregation of PHF-tau. *Science* **370**, eaay8826 (2020).

8   Huryn, D. M., Kornfilt, D. J. P. & Wipf, P. p97: An Emerging Target for Cancer, Neurodegenerative Diseases, and Viral Infections. *J Med Chem.* **63**, 1892-1907 (2020).

9   Skrott, Z. *et al.* Alcohol-abuse drug disulfiram targets cancer via p97 segregase adaptor NPL4. *Nature* **552**, 194-199 (2017).

10 Xia, D., Tang, W. K. & Ye, Y. Structure and function of the AAA+ ATPase p97/Cdc48p. *Gene* **583**, 64-77 (2016).

11 Huyton, T. *et al.* The crystal structure of murine p97/VCP at 3.6 angstrom. *J Struct Biol* **144**, 337-348 (2003).

12 Davies, J. M., Brunger, A. T. & Weis, W. I. Improved structures of full-length p97, an AAA ATPase: Implications for mechanisms of nucleotide-dependent conformational change. *Structure* **16**, 715-726 (2008).

13 Banerjee, S. *et al.* 2.3 A resolution cryo-EM structure of human p97 and mechanism of allosteric inhibition. *Science* **351**, 871-875 (2016).

14 Zhang, X. *et al.* Structure of the AAA ATPase p97. *Mol Cell* **6**, 1473-1484 (2000).

15 Ripstein, Z. A., Huang, R., Augustyniak, R., Kay, L. E. & Rubinstein, J. L. Structure of a AAA+ unfoldase in the process of unfolding substrate. *Elife* **6**, e25754 (2017).

16 Puchades, C. *et al.* Structure of the mitochondrial inner membrane AAA+ protease YME1 gives insight into substrate processing. *Science* **358**, eaao0464 (2017).

17 Zhao, M. L. *et al.* Mechanistic insights into the recycling machine of the SNARE complex. *Nature* **518**, 61-67 (2015).

18 Cooney, I. *et al.* Structure of the Cdc48 segregase in the act of unfolding an authentic substrate. *Science* **365**, 502-505 (2019).

19 Twomey, E. C. *et al.* Substrate processing by the Cdc48 ATPase complex is initiated by ubiquitin unfolding. *Science* **365**, eaax1033 (2019).

20 Alverez, C. *et al.* Allosteric Indole Amide Inhibitors of p97: Identification of a Novel Probe of the Ubiquitin Pathway. *Acs Med Chem Lett.* **7**, 182-187 (2016).

21 Magnaghi, P. *et al.* Covalent and allosteric inhibitors of the ATPase VCP/p97 induce cancer cell death. *Nat Chem Biol.* **9**, 548-556 (2013).

22 Zhang, T., Midshra, P., Hay, B. A., Chan, D. & Guo, M. Valosin-containing protein (VCP/p97) inhibitors relieve Mitofusin-dependent mitochondrial defects due to VCP disease mutants. *Elife* **6**, e17834 (2017).

23 Zhang, J. T. *et al.* Identification of NMS-873, an allosteric and specific p97 inhibitor, as a broad antiviral against both influenza A and B viruses. *Eur J Pharm Sci* **133**, 86-94 (2019).

789   24   Bojkova, D. *et al.* Proteomics of SARS-CoV-2-infected host cells reveals therapy targets.
790   *Nature* **583**, 469-472 (2020).
791   25   Hao, Q. *et al.* A non-canonical role of the p97 complex in RIG-I antiviral signaling. *Embo*
792   *J.* **34**, 2903-2920 (2015).
793   26   Pan, M. *et al.* Seesaw conformations of Npl4 in the human p97 complex and the
794   inhibitory mechanism of a disulfiram derivative. *Nat Commun.* **12**, 121,
795   doi:10.1038/s41467-020-20359-x (2021).
796   27   Blythe, E. E., Gates, S. N., Deshaies, R. J. & Martin, A. Multisystem Proteinopathy
797   Mutations in VCP/p97 Increase NPLOC4.UFD1L Binding and Substrate Processing.
798   *Structure* **27**, 1820-1829 (2019).
799   28   Bodnar, N. O. & Rapoport, T. A. Molecular Mechanism of Substrate Processing by the
800   Cdc48 ATPase Complex. *Cell* **169**, 722-735 (2017).
801   29   Hanzelmann, P. & Schindelin, H. Structural Basis of ATP Hydrolysis and Intersubunit
802   Signaling in the AAA+ ATPase p97. *Structure* **24**, 127-139 (2016).
803   30   Cooney, I. *et al.* Structure of the Cdc48 segregase in the act of unfolding an authentic
804   substrate. *Science* **365**, 502-505 (2019).
805   31   Blythe, E. E., Olson, K. C., Chau, V. & Deshaies, R. J. Ubiquitin- and ATP-dependent
806   unfoldase activity of P97/VCP center dot NPLOC4 center dot UFD1L is enhanced by a
807   mutation that causes multisystem proteinopathy. *Proc Natl Acad Sci USA.* **114**, E4380-
808   E4388 (2017).
809   32   Monroe, N., Han, H., Shen, P. S., Sundquist, W. I. & Hill, C. P. Structural basis of protein
810   translocation by the Vps4-Vta1 AAA ATPase. *Elife* **6**, e24487 (2017).
811   33   Yokom, A. L. *et al.* Spiral architecture of the Hsp104 disaggregase reveals the basis for
812   polypeptide translocation. *Nat Struct Mol Biol.* **23**, 830-837 (2016).
813   34   Song, C., Wang, Q. & Li, C.-C. H. ATPase Activity of p97-Valosin-containing Protein
814   (VCP). *J Biol Chem.* **278**, 3648-3655 (2003).
815   35   Martin, A., Baker, T. A. & Sauer, R. T. Rebuilt AAA+ motors reveal operating principles
816   for ATP-fuelled machines. *Nature* **437**, 1115-1120 (2005).
817   36   Meyer, H. & Weihl, C. C. The VCP/p97 system at a glance: connecting cellular function
818   to disease pathogenesis. *J Cell Sci.* **127**, 3877-3883 (2014).
819   37   Tan, D., Blok, N. B., Rapoport, T. A. & Walz, T. Structures of the double-ring AAA
820   ATPase Pex1/Pex6 involved in peroxisome biogenesis. *FEBS J.* **283**, 986-992 (2015).
821   38   Pickart, C. M. & Raasi, S. Controlled synthesis of polyubiquitin chains. *Methods Enzymol*
822   **399**, 21-36 (2005).
823   39   Zheng, S. Q. *et al.* MotionCor2: anisotropic correction of beam-induced motion for
824   improved cryo-electron microscopy. *Nat Methods* **14**, 331-332 (2017).
825   40   Mindell, J. A. & Grigorieff, N. Accurate determination of local defocus and specimen tilt in
826   electron microscopy. *J Struct Biol* **142**, 334-347 (2003).
827   41   Zivanov, J. *et al.* New tools for automated high-resolution cryo-EM structure
828   determination in RELION-3. *Elife* **7**, e42166 (2018).
829   42   Pettersen, E. F. *et al.* UCSF chimera - A visualization system for exploratory research
830   and analysis. *J Comput Chem* **25**, 1605-1612 (2004).
831   43   Emsley, P. & Cowtan, K. Coot: model-building tools for molecular graphics. *Acta*
832   *Crystallogr D* **60**, 2126-2132 (2004).
833   44   Adams, P. D. *et al.* PHENIX: a comprehensive Python-based system for macromolecular
834   structure solution. *Acta Crystallogr D* **66**, 213-221 (2010).
835